

The discovery of anomalously high levels of [Si/Fe] among metal-poor giants in the bulge, disk, and halo of the Milky Way

José G. Fernández-Trincado^{1,2*}, Timothy C. Beers³, Vinicius M. Placco³, Sarah L. Martell^{4,5}, Edmundo Moreno⁶, Baitian Tang⁷, Alan Alves-Brito⁸, Sandro Villanova⁹, Mario Ortigoza-Urdaneta¹, Dante Minniti^{10,11,12}, Angeles Pérez-Villegas¹³, Céline Rey¹ and Annie C. Robin²

¹*Instituto de Astronomía y Ciencias Planetarias, Universidad de Atacama, Copayapu 485, Copiapo, Chile*

²*Institut Utinam, CNRS UMR6213, Univ. Bourgogne Franche-Comté, OSU THETA, Observatoire de Besançon, BP 1615, 25010 Besançon Cedex, France*

³*Department of Physics and JINA Center for the Evolution of the Elements, University of Notre Dame, Notre Dame, IN 46556, USA*

⁴*School of Physics, University of New South Wales, Sydney NSW 2052*

⁵*Centre of Excellence for Astrophysics in Three Dimensions (ASTRO-3D), Australia*

⁶*Instituto de Astronomía, Universidad Nacional Autónoma de México, Apdo. Postal 70264, México D.F. 04510, México*

⁷*School of Physics and Astronomy, Sun Yat-sen University, Zhuhai 519082, China*

⁸*Universidade Federal do Rio Grande do Sul, Instituto de Física, Av. Bento Gonçalves 9500, Porto Alegre, RS, Brazil*

⁹*Departamento de Astronomía, Casilla 160-C, Universidad de Concepción, Concepción, Chile*

¹⁰*Depto. de Cs. Físicas, Facultad de Ciencias Exactas, Universidad Andrés Bello, Av. Fernández Concha 700, Las Condes, Santiago, Chile*

¹¹*Millennium Institute of Astrophysics, Av. Vicuna Mackenna 4860, 782-0436, Santiago, Chile*

¹²*Vatican Observatory, V00120 Vatican City State, Italy*

¹³*Universidade de São Paulo, IAG, Rua do Matão 1226, Cidade Universitária, São Paulo 05508-900, Brazil*

22nd April 2022

ABSTRACT

Here, we report the discovery of a unique collection of giants, that exhibit anomalously high levels of [Si/Fe] and [Al/Fe] without noticeable carbon and nitrogen enhancement, clearly above typical Galactic levels, distinguishable from dwarf galaxy populations in most chemical elements; their distinction is less apparent among other light-elements such as N and Mg. The newly identified mildly metal-poor sample's [Si/Fe] appear definitively anomalous, having a spread in [Si/Fe] from around +0.6 to +1.1 dex, compared with Galactic [Si/Fe] $\lesssim +0.5$. We confirm that most of the chemically anomalous Si-rich stars are on tight halo-like orbits passing through the bulge, similar to those found in other studies. Their chemical composition is, in general, similar to typical globular cluster stars with extreme abundance, although several differences exist. Furthermore, we did not detect any variation of the radial velocities that would support the binary hypothesis in this unique sample. Thus, the high aluminum and silicon abundances, and enhancements in their *s*-process elements relative to Solar abundance ratios, could be due to formation from gas that was already strongly enriched by SNe II.

Key words: stars: abundances, stars: chemically peculiar, Galaxy: abundances, Galaxy: bulge, globular clusters: general, Galaxy: halo.

1 INTRODUCTION

Mildly metal-poor ($[\text{Fe}/\text{H}] \lesssim -0.7$) field stars with anomalously high abundances of light elements (Al, N, Na and K) with respect to Fe have long been considered polluted stars that have escaped from Galactic and/or extragalactic globular clusters. However, this

paradigm is being challenged, since, apart from unusual elemental abundances in globular cluster environments, a co-eval group of stars in the Galactic field exhibit an intriguing atmospheric composition, which must be understood in terms of whatever nucleosynthetic process producing the anomalous abundance ratios as those invoked to explained the chemical anomalies in globular clusters. This has revived interest in understanding the rare astrophysical events acting to produce such high levels of the light elements, such as the binary channel, which could be responsible for the signal,

* jose.fernandez@uda.cl, jfernandez@obs-besancon.fr, jfernandez87@gmail.com

and if these are related to whatever nucleosynthetic pathway is responsible for the extreme abundance ratios in globular clusters. But, it is now firmly established that field stars showing light-element abundance variations are not exclusive objects of globular-cluster environments.

It has been well-established that a small fraction, $\sim 3\text{--}13\%$ of the local field population of the Milky Way share similar chemical patterns to that the extreme population seen in Galactic and/or extragalactic globular clusters at the same metallicity (see, e.g., Lind et al. 2015; Martell et al. 2016; Fernández-Trincado et al. 2016, 2017; Schiavon et al. 2017; Kemp et al. 2018; Fernández-Trincado et al. 2019; Pereira et al. 2019; Tang et al. 2019; Koch et al. 2019, Fernandez-Trincado et al. 2019b, submitted). Thus, increasing the sample of such field stars is an essential task to identify the mechanism responsible of such chemical anomalies in the Galactic field (see Kemp et al. 2018; Fernández-Trincado et al. 2019, for instance) as well as to help to understand globular cluster formation and evolution. While these authors have quantified the amount of possible *migrants* from globular clusters, their studies often focused in stars with metallicities down to $[\text{Fe}/\text{H}] \sim -0.7$, accompanied by extreme enrichment (higher than $+0.5$ dex) of light-elements such as N, Na, Al and K, and in some case for high levels of *s*-process elements (see e.g., Pereira et al. 2017, Fernandez-Trincado et al. 2019b, submitted), chemistry consistent with the known chemical signature of the so called *second-generation*¹ globular cluster stars, and are now likely the accreted material (relics) from disrupted globular clusters. Thus, their apparent uniqueness in the Galactic field makes this signature an useful chemical "tag" for identifying field stars that possibly escaped from (massive) globular cluster environments (Kruijssen 2015; Lind et al. 2015; Martell et al. 2016; Fernández-Trincado et al. 2016) or from a dwarf galaxy such as Gaia-Enceladus (Belokurov et al. 2018; Helmi et al. 2018) and/or Sagittarius (Hasselquist et al. 2019).

In most cases, such chemical peculiarities have been interpreted as the result of p-capture reactions operating through the nuclear processing of the CNO bi-cycle and/or conversion of ^{24}Mg into ^{27}Al , which may occur during the Mg-Al cycle at temperatures around 75MK (Renzini et al. 2015; Pancino et al. 2017), which is attainable in hot-bottom burning environments of massive- and intermediate-mass asymptotic giant branch (AGB) stars (Ventura et al. 2016; Pereira et al. 2017). In a few cases, it was suggested that anomalously high levels of $[\text{K}/\text{Fe}]$ arose from super-AGB stars (which produces K, destroying Na in the process, e.g., Prantzos et al. 2017; Kemp et al. 2018) could explain the unusual phenomenon in the field. More recent studies focused on sodium-enriched stars, rarely found among metal-poor field stars, which exhibit chemical similarities to second-generation globular cluster stars, implying that it is possible that a high sodium and nitrogen abundance could be related to escaped globular cluster stars or due to metal-poor AGB stars that have experienced strong internal mixing (Pereira et al. 2019), unless they are part of a binary system (Fernández-Trincado et al. 2019). However, an unifying explanation of its origin remains elusive.

To date, a few chemical species like ^{27}Al , ^{14}N , ^{23}Na and ^{39}K appear to play a strong role in identifying chemical anomalies among metal-poor field stars, as well as revealing the phe-

¹ Here, *second-generation* is used to refer to groups of stars showing enhanced N and Al, and depleted C and O abundances, with respect to other field stars at the same metallicity.

nomenon known as "multiple populations" in globular clusters. In this context, a more intriguing aspect seen in globular cluster environments (Mészáros et al. 2015; Masseron et al. 2019), is in their stars along the red horizontal branch (RHB), red giant branch (RGB), and early asymptotic giant branch (eAGB) possess star-to-star variations in Si and Al abundances, with significant Si enhancement for the Al richest stars, i.e., Si-Al are positively correlated with a clear metallicity dependence ($[\text{Fe}/\text{H}] < -1.5$) on the production/depletion yields of the Al source (Masseron et al. 2019). This have been interpreted as a signature of ^{28}Si "leakage" (at metallicities below -2) from Mg-Al chain (Mészáros et al. 2015) or even due to higher temperature in polluters above 75MK (Prantzos et al. 2017), however in metallicities greater than -2 , the mechanism responsible for the puzzling of anomalously high levels of $[\text{Si}/\text{Fe}]$ and $[\text{Al}/\text{Fe}]$ abundances is uncommon among globular clusters and field stars. In this sense, if globular cluster giants display higher $[\text{Si}/\text{Fe}]$ ratios, a dichotomy between field and globular cluster giants may also be expected, implying that ^{28}Si would be another important species useful for chemical tagging of stars that formed in globular clusters, and have since moved to other components of the Milky Way galaxy.

In this Letter we report on the serendipitous discovery of a unique collection of mildly metal-poor ($[\text{Fe}/\text{H}] < -0.7$) field giants with elevated Al and Si, at odds with observations of dwarf galaxies and Milky Way populations, which have chemical similarities to those seen in Galactic globular clusters for most of the chemical species analyzed to date.

2 SI-AL-RICH GIANTS AMONG METAL-POOR STARS

Stars with significantly enhanced aluminum ($[\text{Al}/\text{Fe}] \gtrsim +0.5$) and silicon ($[\text{Si}/\text{Fe}] \gtrsim +0.6$) have thus far only been found in metal-poor globular cluster environments like M15, M92, M53, and M13, and mildly metal-poor clusters like M107 (Masseron et al. 2019). The origin of this abundance signature remains unknown, as does the reason for its apparent exclusivity to these environments. Here we present the discovery of a handful of field giant stars, identified from the $\sim 270,000$ APOGEE giants, that exhibit significantly enhanced $[\text{Si}/\text{Fe}]$ and $[\text{Al}/\text{Fe}]$ abundance ratios. We refer the reader to Appendix A1 and A2 for further details regarding the use of APOGEE spectra and abundance methodology employed in this paper.

Here, we search for high- $[\text{Si}/\text{Fe}]$ outliers in the $[\text{Si}/\text{Fe}]$ – $[\text{Fe}/\text{H}]$ abundance plane, as illustrated in Figure 1, by fitting a 5^{th} order polynomial to stars with standard low- $[\text{Si}/\text{Fe}]$ abundance ratios ($[\text{Si}/\text{Fe}] < +0.6$). We label all stars with silicon abundance that deviate from the fit by $\gtrsim 3\sigma$ from the curve as silicon-rich red-giant stars. The bins were chosen to ensure that at least ~ 100 stars were in each bin. This returns 36 stars that appear Si-rich relative to the full data set. We then eliminate three known globular cluster stars from, leaving 33 Si-rich candidates.

In order to confidently state chemical² tagging results for this data set, we also require enhanced aluminum ($[\text{Al}/\text{Fe}] \gtrsim +0.5$), as a lower aluminum abundance is not by itself a sufficient indicator of a GC-like abundance pattern in the Galactic field. If high levels of Al enrichments are found, this would imply that such Si-Al-rich giant

² We did not include sodium in our analysis, which is a typical species to separate globular cluster populations, as its lines ($1.6373\mu\text{m}$ and $1.6388\mu\text{m}$) in our APOGEE spectra are weak in the typical T_{eff} and metallicity for the star studied in this work, and this would lead to unreliable abundance results.

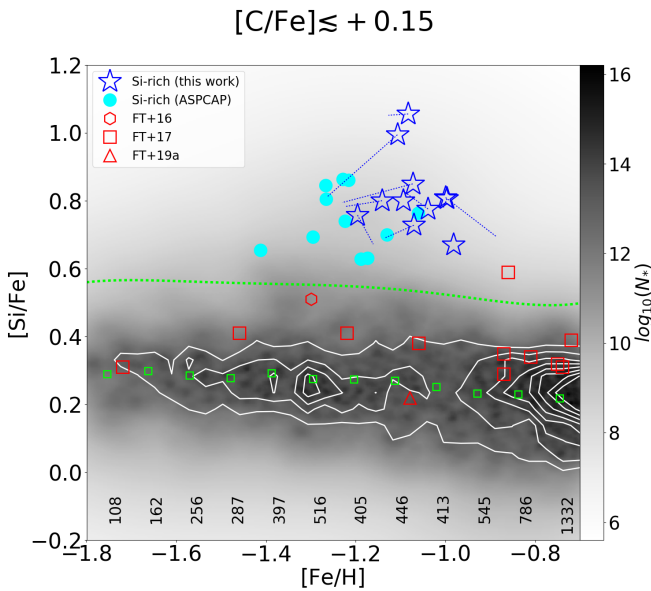


Figure 1. Kernel Density Estimate (KDE) smoothed distribution of [Si/Fe] and [Fe/H] of ASPCAP/APOGEE stars, with the white contours showing the density of objects in the main body of Si-normal stars ($[\text{Si}/\text{Fe}] < +0.6$). The number of stars of each bin are shown at the center of the bin at the inner bottom of the plot, while the open green squares show the mean value of [Si/Fe] by bin. Shown with unfilled blue star symbols are of newly Si-rich stars identified in this study and manually re-analyzed line-by-line adopting the spectroscopy and photometry atmospheric parameters (see text), with blue dotted lines showing the shifted abundance for adopted photometry T_{eff} and estimated surface gravity from 10 Gyr PARSEC isochrones. The ASPCAP/APOGEE abundance of these Si-rich candidates are plotted as cyan symbols. Also shown for comparison are literature N-rich stars manually inspected from FT16 (unfilled hexagon), FT17 (unfilled squares) and FT19 (unfilled triangle) in the same manner as the present work.

field stars and *second-generation* globular cluster stars could potentially be the same kind of stellar objects, with similar nucleosynthetic histories. This leaves us with 11 likely Si-Al-rich red-giants with high-quality spectra and reliable parameters and abundances. For most of the newly identified Si-rich stars there are no known globular clusters within an angular separation of 0.5 degree.

A comparison is presented in Figure A1, where the spectra of a Si-rich and a Si-normal star are shown in the relevant wavelength range containing the Si I lines, indicated by vertical tick marks. The Si-rich star has remarkably stronger Si I lines which, in view of the similarity between the two stars in all the other relevant parameters, can only mean that it has a much higher silicon abundance. Both ASPCAP (García Pérez et al. 2016) and our line-by-line manual analysis with BACCHUS tell us that [Si/Fe] in the Si-rich star is higher than the Si-normal star by 0.4 dex. None of the eleven Si-rich stars without strong carbon enhancement have a particularly strong enrichment in nitrogen, which make them an unique collection of stars within of the family of chemically anomalous field stars (Martell et al. 2016; Fernández-Trincado et al. 2016; Schiavon et al. 2017; Fernández-Trincado et al. 2017, 2019). In doing chemical tagging in the disk (thick), we have moved past just asking whether stars could have formed in globular clusters, and now we are looking for ways to understand several different types of chemically anomalous stars.

3 RESULTS AND DISCUSSION

We have discovered the first eleven Si-rich stars in the Galactic field, with an unexpected and exceptional enhancement of ^{28}Si among mildly metal-poor stars. The [Si/Fe] abundance reported here are significantly above the typical value measured in the Milky Way, but also higher than the value seen in globular cluster stars in given metallicity. The origin of Si-rich stars is unclear and can be ascribed to different processes.

3.1 Chemical Signature of the Si-rich Giants

Figure 1 strongly suggests the existence of a population of stars chemically differentiated by their [Si/Fe] patterns, clumped at values $[\text{Si}/\text{Fe}] > +0.6 - +1.1$, at metallicities as low as $[\text{Fe}/\text{H}] \sim -0.8$ and -1.1 , nominally below the metal-poor tail of the canonical thick-disk metallicity distribution. Additionally, close inspection of Figure 1 reveals that the main body (white contours) of Si-normal stars for $[\text{Si}/\text{Fe}] < +0.6$ may be canonical disk and halo stars.

Now we turn our attention to the high [Si/Fe] outliers in Figure 1. A diagnostic plot that can shed light on the nature of these stars is shown in Figure 2, where Si-rich stars are again highlighted by blue unfilled 'star' symbols. One can see that the Si-rich stars are distributed in discrete regions in the planes N-Al and Mg-Al, clumped at values greater than $+0.5$ in their [Al/Fe] ratios, and with [N/Fe] as low as $\sim +0.5$, which clearly differs from that of nitrogen-enhanced ($[\text{N}/\text{Fe}] \gtrsim +0.5$) field giants, which have been analyzed manually in Fernández-Trincado et al. (2016, 2017, 2019) in the same manner as the present study, and differ from the thick-disk and halo abundance pattern. This suggest that, at least at higher aluminum abundance ratios ($[\text{Al}/\text{Fe}] \gtrsim +0.5$) among metal-poor giants (< -0.7) globular cluster stars like those found throughout the Milky Way, are likely to contribute to the anomalously high levels of [Si/Fe] in the Galactic field.

Regarding magnesium, the [Mg/Fe] abundance ratios of the S-rich stars exhibit a small (~ 0.25 dex), similar to what is seen in the literature for the thick disk or "high-Mg" population claimed to have a *in situ* formation origin Hayes et al. (2018). However, their larger orbital eccentricities, clumped at values greater than $e = 0.65$, accompanied by their large enrichment in Al and Si, suggest that most these stars are unlikely to be members of the canonical thick disk or halo. It is also clear in Figure 2 that [Al/Fe] presents the largest distinction between the main body of the Milky Way stars and other anomalous stars. The rest of the chemical abundances ([N/Fe] and [Mg/Fe]) appear to be very mixed, making it difficult to disentangle from the rest of the Milky Way population.

The third and fourth panel in Figure 2 show the trends of [N/Fe] and [Mg/Fe] with metallicity, where clearly, N abundance is slightly deficient, and might represent an intermediate (at $[\text{N}/\text{Fe}] \sim +0.3$), transitional stage between the anomalously high levels of [N/Fe] (red unfilled symbols) and the main body of the Milky Way. On the other hand, [Mg/Fe] abundance ratios are relatively scattered towards higher metallicities for the newly identified stars. We would conclude that in key elemental abundance space (namely C, N, Al, Mg, and Fe) the Si-rich stars, the literature N-rich stars, the disk-thick and halo populations may comprise similar objects at a given iron abundance. They may not be typical disk-thick and/or halo stars, but they also are not typical stars as seen in dwarf galaxies, as massive dwarf galaxies like the Sagittarius dwarf spheroidal galaxy does not contain stars with higher aluminum abundance ratios, $[\text{Al}/\text{H}] \gtrsim +0.5$ (e.g., Hasselquist et al. 2017, 2019, and references therein).

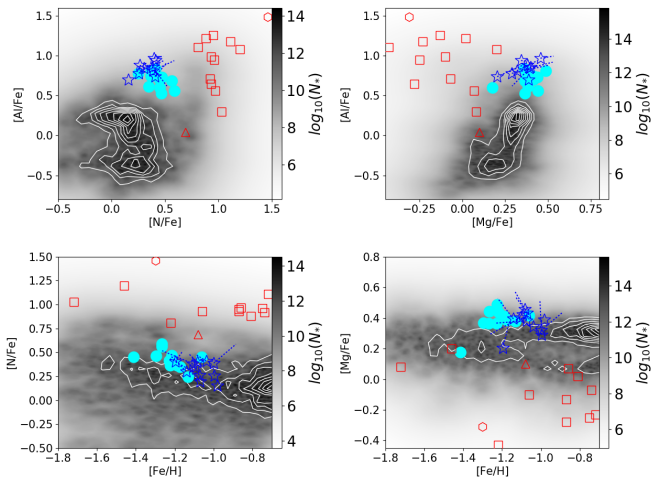


Figure 2. Kernel Density Estimate (KDE) smoothed distribution of $[Al/Fe]$, $[N/Fe]$, $[Mg/Fe]$ and $[Fe/H]$ of ASPCAP/APOGEE-2s stars. The symbols have the same meaning as those in Figure 1.

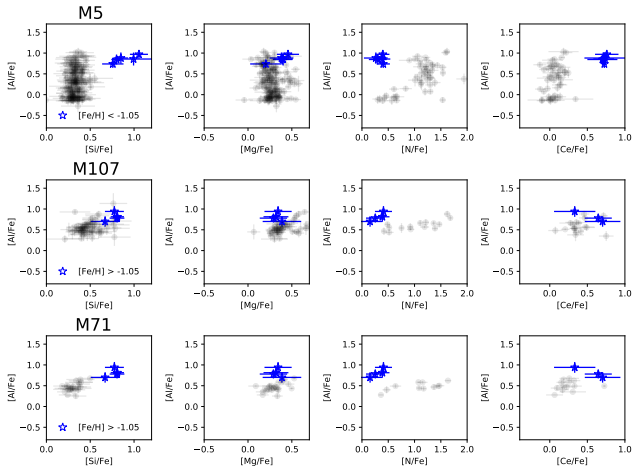


Figure 3. M5, M107, and M71 stars from (Masseron et al. 2019) are shown as filled grey dots in the Si-Al, Mg-Al, N-Al, and Ce-Al planes. The crosses indicate typical error bars. The Si-Al-rich stars are indicated with blue 'star' symbols.

There are also oxygen abundances provided for our sample, listed in Table A2. We urge caution about the accuracy of $[O/Fe]$, as they display larger scatter, which may be due to telluric features and uncertain determinations in the T_{eff} regime of our objects. As we have already highlighted in Fernandez-Trincado et al. (2019b), the uncertainty arises because BACCHUS determines these abundances from the strengths of $^{12}\text{C}^{14}\text{N}$ and $^{12}\text{C}^{16}\text{O}$ lines, which become too weak for stars at relatively low metallicities ($[Fe/H] \lesssim -0.7$).

It is interesting to note that there are nine Si-rich stars that have mildly enhanced values of neutron-capture elements $[Ce/Fe]$ and $[Nd/Fe]$ ($\sim 0.3 - 0.8$), which appears to be correlated with large increases in the Al abundance, except for a few stars, suggesting that the Ce and Nd we have measured could have a pure s -process origin. Binary mass transfer from an intermediate-mass

($M \sim 3 - 4 M_{\odot}$) AGB star can cause high surface abundances of s -process elements (Cristallo et al. 2015), and this material can be transferred onto a binary companion if the physical conditions are appropriate (orbital separation, etc.), thus the companion star's atmosphere reflect the signature of AGB nucleosynthesis, which persists to the present day. However, combining the absence of radial velocity variations ($RV_{\text{SCATTER}} < 0.5 \text{ km s}^{-1}$ as listed in Table A1), no carbon enrichment, and silicon over-abundances, we conclude that such stars are not members of binary systems, and it is possible that mass transfer did not happen in the past. Some Galactic globular clusters also exhibit interesting enrichment in s -process elements (e.g., Masseron et al. 2019) and anomalously high levels of light elements like our sample. In fact, most of the stars in our sample replicate (or exceed) the extreme abundance patterns of Galactic globular clusters, highlighting the uniqueness of these environments, as seen in Figure 3. We leave a fuller discussion of the use of s -process abundances in chemical tagging of globular cluster stars for a future study.

Figure 3 displays the same data and symbols plotted in Figure 1, compared with those obtained from a run of BACCHUS for globular cluster stars (Masseron et al. 2019) at the same metallicity as our objects. Remarkably, most (7/11) of the newly identified Si-rich field stars have light- and heavy-element abundances that appear too high, together with their low $[N/Fe]$ abundance ratios, to be associated with observations of globular cluster stars at lower metallicities ($[Fe/H] \lesssim -1.05$), while a few (4/11) of these Si-rich giants may have chemical abundance similar to the globular cluster population at high metallicities ($[Fe/H] > -1.05$), and provides strong evidence either for the uniqueness of the progenitor stars to globular clusters, while the more metal-poor Si-rich giant stars represents an unique collection of field stars. It seems likely that whatever process is responsible for this subgroup of anomalous field stars differs from whatever caused the unusual stellar populations in metal-poor globular clusters.

One possible polluter but invoking an external production of ^{28}Si (enriching the ISM) is due to massive super novae ($M > 20 M_{\odot}$), pair-instability supernova (PISNs), hypernovae (with stellar progenitors masses greater than $> 140 M_{\odot}$), and/or faint supernovae (Nomoto et al. 2006; Heger & Woosley 2010; Nomoto et al. 2013), which seems to indicate that the newly identified Si-rich giants formed from gas already strongly enriched from these objects. Thus, the anomalously high levels of $[Si/Fe]$ may be a result of the enrichment from explosive nucleosynthesis of core-collapse supernovae (SNe II) events, which can explain the abundance feature of the Si-rich giants.

In Appendix A3 we provide a complementary orbital study of our 11 stars identified as Si-rich throughout the Milky Way.

4 CONCLUSIONS

In this work, we presented the analysis of selected APOGEE-2/DR14 spectra, which reveal the existence of an unique collection of chemically peculiar giants throughout the Milky Way. These stars show anomalously high levels of silicon ($[Si/Fe] \gtrsim +0.5$) when compared to metal-poor field stars at the same metallicity range. The more metal-rich ($[Fe/H] \gtrsim -1.05$) stars in our sample are good candidates to be stars that escaped from globular clusters, whereas their metal-poor ($[Fe/H] < -1.05$) counterparts, which display unusual abundance patterns in ^{28}Si , do not seem to share the same origin.

We speculate that these results indicate the presence of a pop-

ulation of dissolved globular cluster stars with anomalously high levels of [Si/Fe] in the Milky Way field. However, the signature α -element abundance pattern associated with a pair-instability supernova (PISNs), hypernovae, and/or faint supernovae (where ^{28}Si is enhanced), appears to be present in the newly identified Si-rich population, making these possible polluter candidates. Even though the [Si/Fe] abundance ratios match those of a medium polluted by SNe II qualitatively, additional statistics on these stars is needed to confirm these predictions. A handful of the Si-rich/ α -rich stars are thought to be formed in regions of the Milky Way galaxy where SNII were numerous, thus in a significantly higher star formation region than the α -poor stars (e.g., Hawkins et al. 2015).

Furthermore, the orbital integration indicates that the Si-rich stars selected in this work possess halo-like orbits passing through the bulge and disk of the Milky Way. It is also possible that a few of them have been accreted from Galactic globular clusters. The discovery of such peculiar giants indicates that, while almost all Si-rich stars currently reside in the Galactic (inner) halo, they were not necessarily formed in the halo. The radial-velocity data available does not provide enough information to support the hypothesis of such objects possibly being formed in a binary system.

This initial APOGEE-2 sample significantly contributes to the task of compiling a more thorough census of the chemically anomalous stars throughout the Milky Way and portends promising results to be expected from future spectroscopic follow-up observations. Thus, a future inventory of the chemistry of these stars, in particular, the elements formed by neutron-capture processes, would hint at their origin, and possibly help confirm or refute the association with Galactic globular cluster stars.

References

Abolfathi B., et al., 2018, *ApJS*, **235**, 42
 Alvarez R., Plez B., 1998, *A&A*, **330**, 1109
 Aoki W., Beers T. C., Christlieb N., Norris J. E., Ryan S. G., Tsangarides S., 2007, *ApJ*, **655**, 492
 Arenou F., et al., 2018, *A&A*, **616**, A17
 Belokurov V., Erkal D., Evans N. W., Koposov S. E., Deason A. J., 2018, *MNRAS*, **478**, 611
 Blanton M. R., et al., 2017, *AJ*, **154**, 28
 Bressan A., Marigo P., Girardi L., Salasnich B., Dal Cero C., Rubele S., Nanni A., 2012, *MNRAS*, **427**, 127
 Brunthaler A., et al., 2011, *Astronomische Nachrichten*, **332**, 461
 Cristallo S., Straniero O., Piersanti L., Gobrecht D., 2015, *ApJS*, **219**, 40
 Cunha K., et al., 2017, *ApJ*, **844**, 145
 Fernández-Trincado J. G., et al., 2015, *A&A*, **583**, A76
 Fernández-Trincado J. G., et al., 2016, *ApJ*, **833**, 132
 Fernández-Trincado J. G., et al., 2017, *ApJL*, **846**, L2
 Fernández-Trincado J. G., et al., 2018, arXiv e-prints, Fernández-Trincado J. G., et al., 2019, arXiv e-prints, García Pérez A. E., et al., 2016, *AJ*, **151**, 144
 González Hernández J. I., Bonifacio P., 2009, *A&A*, **497**, 497
 Gunn J. E., et al., 2006, *AJ*, **131**, 2332
 Gustafsson B., Edvardsson B., Eriksson K., Jørgensen U. G., Nordlund Å., Plez B., 2008, *A&A*, **486**, 951
 Harris W. E., 1996, *AJ*, **112**, 1487
 Hasselquist S., et al., 2016, *ApJ*, **833**, 81
 Hasselquist S., et al., 2017, *ApJ*, **845**, 162
 Hasselquist S., et al., 2019, *ApJ*, **872**, 58
 Hawkins K., Jofré P., Masseron T., Gilmore G., 2015, *MNRAS*, **453**, 758
 Hawkins K., Masseron T., Jofré P., Gilmore G., Elsworth Y., Hekker S., 2016, *A&A*, **594**, A43
 Hayes C. R., et al., 2018, *ApJ*, **852**, 49
 Heger A., Woosley S. E., 2010, *ApJ*, **724**, 341
 Helmi A., Babusiaux C., Koppelman H. H., Massari D., Veljanoski J., Brown A. G. A., 2018, *nat*, **563**, 85
 Holtzman J. A., et al., 2015, *AJ*, **150**, 148
 Holtzman J. A., et al., 2018, *AJ*, **156**, 125
 Jönsson H., et al., 2018, *AJ*, **156**, 126
 Kemp A. J., et al., 2018, *MNRAS*, **480**, 1384
 Koch A., Grebel E. K., Martell S. L., 2019, arXiv e-prints, Kruijssen J. M. D., 2015, *MNRAS*, **454**, 1658
 Leung H. W., Bovy J., 2019, arXiv e-prints, Lind K., et al., 2015, *A&A*, **575**, L12
 Lindegren L., et al., 2018, *A&A*, **616**, A2
 Lucatello S., Beers T. C., Christlieb N., Barklem P. S., Rossi S., Marsteller B., Sivarani T., Lee Y. S., 2006, *ApJL*, **652**, L37
 Majewski S. R., Zasowski G., Nidever D. L., 2011, *ApJ*, **739**, 25
 Majewski S. R., et al., 2017, *AJ*, **154**, 94
 Martell S. L., et al., 2016, *ApJ*, **825**, 146
 Masseron T., Merle T., Hawkins K., 2016, BACCHUS: Brussels Automatic Code for Characterizing High accUracy Spectra, Astrophysics Source Code Library (ascl:1605.004), doi:10.20356/C4TG6R
 Masseron T., et al., 2019, *A&A*, **622**, A191
 Mészáros S., et al., 2015, *AJ*, **149**, 153
 Minniti D., Fernández-Trincado J. G., Ripepi V., Alonso-García J., Contreras Ramos R., Marconi M., 2018, *ApJL*, **869**, L10
 Nidever D. L., et al., 2015, *AJ*, **150**, 173
 Nomoto K., Tominaga N., Umeda H., Kobayashi C., Maeda K., 2006, *Nuclear Physics A*, **777**, 424
 Nomoto K., Kobayashi C., Tominaga N., 2013, *ARA&A*, **51**, 457
 Pancino E., et al., 2017, *A&A*, **601**, A112
 Pereira C. B., Smith V. V., Drake N. A., Roig F., Hasselquist S., Cunha K., Jilinski E., 2017, *MNRAS*, **469**, 774
 Pereira C. B., Holanda N., Drake N. A., Roig F., 2019, *AJ*, **157**, 70
 Pérez-Villegas A., Portail M., Gerhard O., 2017, *MNRAS*, **464**, L80
 Pérez-Villegas A., Rossi L., Ortolani S., Casotto S., Barbuy B., Bica E., 2018, *Publ. Astron. Soc. Australia*, **35**, e021
 Plez B., 2012, Turbospectrum: Code for spectral synthesis, Astrophysics Source Code Library (ascl:1205.004)
 Prantzos N., Charbonnel C., Iliadis C., 2017, *A&A*, **608**, A28
 Renzini A., et al., 2015, *MNRAS*, **454**, 4197
 Schiavon R. P., et al., 2017, *MNRAS*, **465**, 501
 Smith V. V., et al., 2013, *ApJ*, **765**, 16
 Tang B., Liu C., Fernández-Trincado J. G., Geisler D., Shi J., Zamora O., Worthey G., Moreno E., 2019, *ApJ*, **871**, 58
 Taylor M. B., 2005, in Shopbell P., Britton M., Ebert R., eds, Astronomical Society of the Pacific Conference Series Vol. 347, Astronomical Data Analysis Software and Systems XIV. p. 29
 Ventura P., et al., 2016, *ApJL*, **831**, L17
 Zamora O., et al., 2015, *AJ*, **149**, 181
 Zasowski G., et al., 2013, *AJ*, **146**, 81
 Zasowski G., et al., 2017, *AJ*, **154**, 198

ACKNOWLEDGMENTS

We thank Szabolcs Mészáros for helpful support computing the photometry T_{eff} , and especially grateful for the technical expertise and assistance provided by the Instituto de Astrofísica de Canarias (IAC). This article is based upon work from the ChETEC COST Action (CA16117), supported by COST (European Cooperation in Science and Technology). J.G.F-T is supported by FONDECYT No. 3180210. J.G.F-T acknowledges the use of TOPCAT (Taylor 2005) through out the course of this investigation. T.C.B. acknowledge partial support for this work from grant PHY 14-30152; Physics Frontier Center / JINA Center for the Evolution of the Elements (JINA-CEE), awarded by the US National Science Foundation. B.T. acknowledges support from the one-hundred-talent project of

Sun Yat-Sen University. SLM acknowledges funding from the Australian Research Council through Discovery grant DP180101791, and from the UNSW Scientia Fellowship program. Parts of this research were conducted by the Australian Research Council Centre of Excellence for All Sky Astrophysics in 3 Dimensions (ASTRO 3D), through project number CE170100013. SV gratefully acknowledges the support provided by Fondecyt reg. n. 1170518. A.P-V acknowledges a FAPESP for the postdoctoral fellowship grant no. 2017/15893-1 and the DGAPA-PAPIIT grant IG100319.

BACCHUS have been executed on computers from the Utinam Institute of the Université de Franche-Comté, supported by the Région de Franche-Comté and Institut des Sciences de l'Univers (INSU).

Funding for the *GravPot16* software has been provided by the Centre national d'études spatiales (CNES) through grant 0101973 and UTINAM Institute of the Université de Franche-Comté, supported by the Région de Franche-Comté and Institut des Sciences de l'Univers (INSU). Simulations have been executed on computers from the Utinam Institute of the Université de Franche-Comté, supported by the Région de Franche-Comté and Institut des Sciences de l'Univers (INSU), and on the supercomputer facilities of the Mésocentre de calcul de Franche-Comté.

Funding for the Sloan Digital Sky Survey IV has been provided by the Alfred P. Sloan Foundation, the U.S. Department of Energy Office of Science, and the Participating Institutions. SDSS-IV acknowledges support and resources from the Center for High-Performance Computing at the University of Utah. The SDSS web site is www.sdss.org. SDSS-IV is managed by the Astrophysical Research Consortium for the Participating Institutions of the SDSS Collaboration including the Brazilian Participation Group, the Carnegie Institution for Science, Carnegie Mellon University, the Chilean Participation Group, the French Participation Group, Harvard-Smithsonian Center for Astrophysics, Instituto de Astrofísica de Canarias, The Johns Hopkins University, Kavli Institute for the Physics and Mathematics of the Universe (IPMU) / University of Tokyo, Lawrence Berkeley National Laboratory, Leibniz Institut für Astrophysik Potsdam (AIP), Max-Planck-Institut für Astronomie (MPIA Heidelberg), Max-Planck-Institut für Astrophysik (MPA Garching), Max-Planck-Institut für Extraterrestrische Physik (MPE), National Astronomical Observatory of China, New Mexico State University, New York University, University of Notre Dame, Observatório Nacional / MCTI, The Ohio State University, Pennsylvania State University, Shanghai Astronomical Observatory, United Kingdom Participation Group, Universidad Nacional Autónoma de México, University of Arizona, University of Colorado Boulder, University of Oxford, University of Portsmouth, University of Utah, University of Virginia, University of Washington, University of Wisconsin, Vanderbilt University, and Yale University.

APPENDIX A: SUPPLEMENTARY INFORMATION

A1 APOGEE data selection

The stars analysed in this work consist of red giants from the 14th data release of SDSS (Abolfathi et al. 2018; Jönsson et al. 2018; Holtzman et al. 2018), which includes results from the APOGEE-2 survey (Majewski et al. 2017). This sample has available high-resolution ($R \sim 22,500$) spectra of $\sim 270,000$ stars in the H -band ($\sim 1.5\text{--}1.7\mu\text{m}$), obtained with the 300-fiber cryogenic spectrograph installed on the 2.5m Telescope (Gunn et al. 2006) at the Apache Point Observatory as part of the Sloan Digital Sky Survey IV (Blanton et al. 2017). Targeting strategies for APOGEE and APOGEE-2, data reduction of the APOGEE spectra, and determination of radial velocities, atmospheric parameters, and stellar abundances are fully described in previous work; (Zasowski et al. 2013, 2017; Nidever et al. 2015; Zamora et al. 2015; Holtzman et al. 2015), and (García Pérez et al. 2016), respectively.

Since we are primarily interested in abundance anomalies of metal-poor stars, our focus in this work is on giants with metallicities as low as $[\text{Fe}/\text{H}] < -0.7$, i.e., below the metal-poor tail of the canonical thick disk. We selected a sample of giants, adopting conservative cuts on the columns of the APOGEE-2 catalogue in the following way: (i) $\text{S/N} > 70 \text{ pixel}^{-1}$; (ii) $3500 \text{ K} < \text{T}_{\text{eff}} < 6000 \text{ K}$; (iii) $\log g < 3.6$; and (iv) $\text{ASPCAPFLAG}^3 = 0$.

Following the conventions in the literature, we require non-enhanced carbon stars with $[\text{C}/\text{Fe}] < +0.15$ (e.g., Martell et al. 2016; Fernández-Trincado et al. 2016, 2017, 2019; Masseron et al. 2019), because such stars are commonly found in globular clusters, and the surface abundance of stars enhanced in carbon ($[\text{C}/\text{Fe}] > +0.15$) may have been modified by mass transfer from an AGB companions (e.g., Lucatello et al. 2006; Aoki et al. 2007). The initial sample contained 5,653 stars restricted to the metallicity regions $-1.8 \lesssim [\text{Fe}/\text{H}] \lesssim -0.7$. By requiring metallicity below -0.7 we minimize the presence of giants in the thin and thick disk, and by imposing a lower limit on metallicity of -1.8 , allow for the inclusion of stars with reliable carbon and nitrogen abundances (Mészáros et al. 2015; Martell et al. 2016; Fernández-Trincado et al. 2016, 2017, 2018, 2019).

A2 Line-by-line abundance methodology

In order to examine the reliability of the high-[Si/Fe] outliers, we made a careful inspection of each APOGEE spectrum. We made use of the Brussels Automatic Stellar Parameter (BACCHUS) code (Masseron et al. 2016) to derive the metallicity, broadening parameters, and chemical abundances for the Si-rich sample, based on a careful line selection, as well as providing abundances based on a line-by-line differential approach.

The BACCHUS pipeline relies on the radiative transfer code Turbospctrum (Alvarez & Plez 1998; Plez 2012) and the MARCS model atmosphere grid (Gustafsson et al. 2008). For each element and each line, the abundance determination proceeds as in (Hawkins et al. 2016) and (Fernández-Trincado et al. 2019), and summarized here for guidance: (i) a spectrum synthesis, using the full set of (atomic and molecular) lines, is used to find the local continuum level via a linear fit; (ii) cosmic and telluric rejections are performed; (iii) the local S/N is estimated; (iv) a series of flux

³ This cut ensure that there were no major flagged issues, i.e., low S/N, poor synthetic spectral fit, stellar parameters near grid boundaries, among other.

points contributing to a given absorption line is automatically selected; and (v) abundances are then derived by comparing the observed spectrum with a set of convolved synthetic spectra characterised by different abundances. Four different abundance determinations are used: (i) line-profile fitting; (ii) core line intensity comparison; (iii) global goodness-of-fit estimate; and (iv) equivalent width comparison. Each diagnostic yields validation flags. Based on these flags, a decision tree then rejects the line or accepts it, keeping the best-fit abundance. We adopted the χ^2 diagnostic as the abundance because it is the most robust. However, we store the information from the other diagnostics, including the standard deviation between all four methods. The linelist used in this work is the latest internal DR14 atomic/molecular linelist (linelist.20170418). For a more detailed description of these lines, we refer the reader to a forthcoming paper (Holtzman et al. in preparation). The current version of ASPCAP/DR14 does not determine the *s*-process elements (Nd II and Ce II), thus we determinates these elements in our target stars adopting the linelist as provided in (Hasselquist et al. 2016) and (Cunha et al. 2017).

In particular, a mix of heavily CN-cycled and α -poor MARCS models were used, as well as the same molecular lines adopted by (Smith et al. 2013), were employed to determine the C, N, and O abundances. In addition, we have adopted the C, N, and O abundances that satisfy the fitting of all molecular lines consistently; i.e., we first derive ^{16}O abundances from ^{16}OH lines, then derive ^{12}C from $^{12}\text{C}^{16}\text{O}$ lines and ^{14}N from $^{12}\text{C}^{14}\text{N}$ lines; the CNO abundances are derived several times to minimize the OH, CO, and CN dependences (Smith et al. 2013; Fernández-Trincado et al. 2018, 2019).

In order to provide a consistent chemical analysis, we re-determine the chemical abundances, assuming as input the uncalibrated effective temperature (T_{eff}), surface gravity ($\log g$), and metallicity ($[\text{M}/\text{H}]$) as derived by ASPCAP/APOGEE runs. We also applied a simple approach of fixing $\text{T}_{\text{eff}}^{\text{phot}}$ and $\log g$ to values, determined independently of spectroscopy, in order to check for any significant deviation in the chemical abundances. For this, the photometric effective temperatures were calculated from the $J_{2\text{MASS}} - K_{s,2\text{MASS}}$ color relation using the methodology presented in (González Hernández & Bonifacio 2009). Photometry is extinction-corrected using the Rayleigh Jeans Color Excess (RJCE) method (Majewski et al. 2011). We estimate surface gravity from 10 Gyr PARSEC (Bressan et al. 2012) isochrones, as 10 Gyr is the typical age of Galactic GCs (Harris 1996); here we are clearly assuming that such Si-rich stars could be globular cluster migrants. The adopted stellar parameters are listed in Table A1.

Figure A2 compares the difference between the adopted atmospheric parameters. The average of these differences were found to be negligible for the uncalibrated ASPCAP/APOGEE temperatures and photometry temperatures ($< 10 \text{ K}$), but significantly higher in $\log g$ ($\sim 0.5 \text{ dex}$), as illustrated in the top panel at the same figure. However, for a few stars, the uncalibrated ASPCAP/APOGEE raw temperature above 4500 K in metal-poor stars showed significant, $\sim 250 \text{ K}$ offsets, compared to photometry with low surface gravity offsets ($< 0.25 \text{ dex}$) in the same temperature range, while ASPCAP/APOGEE uncalibrated temperatures below 4500 K in metal-poor stars showed significant, $0.2 - 0.5 \text{ dex}$ offsets, compared to photometry, and are thus believed to exhibit large scatter in the abundance analysis for several elements, as seen at the same figure. This issue does not affect the derived $[\text{Si, Al}/\text{Fe}] > +0.5$, where the vast majority of our APOGEE targets are as illustrated in Figure A2. All of the chemical species presented in this figure have been

re-determined adopting a line-by-line abundance analysis with the BACCHUS code.

Figure A2 also indicates that the BACCHUS code recovers the [Fe/H] abundance ratios of these stars within ~ 0.15 dex for both adopted photometric and spectroscopic temperatures. The adoption of a purely photometry temperature scale enables us to be somewhat independent of ASPCAP/APOGEE pipeline, which provides important comparison data for future pipeline validation. The final results presented in this paper are based on computations done with the BACCHUS code using both the spectroscopy and photometry temperatures, while the reported uncertainty is based in the adopted spectroscopy atmospheric parameters, which is defined as:

$$\sigma_{total}^2 = \sigma_{[X/H], T_{eff}}^2 + \sigma_{[X/H], \log g}^2 + \sigma_{[X/H], \xi_t}^2 + \sigma_{mean}^2 \quad (\text{A1})$$

where σ_{mean}^2 is calculated using the classical standard deviation derived from the different abundances of the different lines for each element. $\sigma_{[X/H], T_{eff}}^2$, $\sigma_{[X/H], \log g}^2$ and $\sigma_{[X/H], \xi_t}^2$ are derived for each element and each star using the sensitivity values of ± 100 K for the temperature, ± 0.3 dex for $\log g$, and 0.05 km s^{-1} for the microturbulent velocity (ξ_t).

Figure A3 show examples of observed Si I line profiles and their fitted LTE synthesis using the BACCHUS code for the eleven stars reported in this work. The wavelength regions shown in this figure cover the full linelist used to obtained the final [Si/Fe] abundance ratios, where an average [Si/Fe] is listed in Table A2. Although the BACCHUS pipeline has its own procedure to include or reject lines on a star-by-star basis, it is still important to select the lines beforehand, because of the uncertainty related to the synthesis approach, such as line saturation among other. The selected Si I lines were visually inspected to ensure that the spectral fit was adequate.

A3 Galactic orbits

We estimate the probable Galactic orbits for the eleven Si-Al-rich stars analyzed in this study, in order to provide insights on the origin of such stars throughout the Milky Way. For this, we combine precise proper motions from Gaia DR2 (Arenou et al. 2018; Lindegren et al. 2018), radial velocity from APOGEE (Nidever et al. 2015) and precise spectro-photometric distances from Leung & Bovy (2019) as input data in the new state-of-the-art orbital integration package GravPot16⁴. The Galactic potential assumed in these calculations was the non-axisymmetric Milky Way-like potential, which considers perturbations due to a realistic (as far as possible) rotating boxy/peanut bar, which fits the structural and dynamical parameters of the Galaxy, based on to the best we know of the recent knowledge of our Milky Way. Here, we provide orbital solutions assuming four different values of the angular velocity of the bar, $\Omega_{bar} = 35, 40, 45, \text{ and } 50 \text{ km s}^{-1} \text{ kpc}^{-1}$, with a bar mass of $1.1 \times 10^{10} M_{\odot}$, and a present-day angle orientation of 20° , in the same mannear as Fernández-Trincado et al. (2019). To model the uncertainty distributions, we sampled one million orbits using a Monte Carlo approach, assuming a normal distribution for the uncertainties of the input parameters (positions, distances, radial velocities and proper motions). The results are listed in Table A5, the data presented in this table correspond to a backward time integration of 3 Gyr. In this table, we listed the sign of the z-component of the angular momentum in the inertial fram, L_z , since this quantity

is not conserved in a model like GravPot16 and we are interested in the variation of L_z along the full integration time, i.e., in the prograde and/or retrograde sense with respect to the rotation of the bar.

For reference, the Galactic convention adopted by this work is: X –axis is oriented toward $l = 0^\circ$ and $b = 0^\circ$, and the Y –axis is oriented toward $l = 90^\circ$ and $b = 0^\circ$, and the disc rotates toward $l = 90^\circ$; the velocities are also oriented in these directions. In this convention, the Sun’s orbital velocity vector are $[U_{\odot}, V_{\odot}, W_{\odot}] = [11.1, 12.24, 7.25] \text{ km s}^{-1}$ (Brunthaler et al. 2011). The model has been rescaled to the Sun’s galactocentric distance, 8.3 kpc, and a local rotation velocity of 239 km s^{-1} (e.g., Brunthaler et al. 2011).

Figure A4 illustrates the coverage of the eleven Si-rich giants in an Aitoff projection in Galactic coordinates in the footprint of the APOGEE-2 survey. The newly discovered stellar population spans a large range in heliocentric distances, $3 < d < 12$ kpc, more likely found at intermediate to high latitudes $|b| > 10^\circ$, with a few exceptions to the inner regions of the Milky Way, as seen in the same figure. An orbital integration of these stars was performed, and showed that many of them have high eccentricity, which appear to behave as halo-like orbits, some of which have *mid-* and *off-plane* orbits passing through the inner Galaxy. However, we find that these are not stars that live in the inner regions like some bulge globular clusters and/or older stars (Pérez-Villegas et al. 2018; Min-niti et al. 2018).

Figure A6 shows the distributions of each orbital parameter, for the non-axisymmetric configuration of GravPot16, assuming a $\Omega_{bar} = 35\text{--}50 \text{ km s}^{-1}$. The newly discovered giants are found to have radial orbits, with pericentre values less than 2 kpc, apocentre values ranging between 4–24 kpc, eccentricities larger than 0.65, and maximum vertical excursion from the Galactic plane ranging between 0.5–20 kpc. The orbital parameters clearly show that most of these giants do not live in the inner Galaxy, and therefore those identified toward the bulge region are likely halo intruders into the inner Galaxy like, e.g., 2M18070782–1517393, whose orbit move around the co-rotation (CR) region, except 2M17502038–2805411, which has a bar-shape orbit in the (X–Y) projection, and shares the orbital properties of the bar/bulge; this indicates that this star was likely trapped by some resonance of the bar.

It is also important to mention that 5 out of 11 Si-rich stars exhibit retrograde orbits, compared with the other Si-rich stars and appear to have halo-like orbits (Pérez-Villegas et al. 2017, 2018). It is possible that a few of these giants are the stripped material of Galactic globular clusters (like ω Cen, among others). This provides observational support for the idea that the mildly metal-poor ($[\text{Fe/H}] \lesssim -0.7$) stars in the inner Galactic halo may have been assembled by kicking out Galactic globular cluster stars (Fernández-Trincado et al. 2015, 2016).

These dynamical properties suggest that most of the Si-rich giants were likely formed during the very early stages of the evolution of the Milky Way, in a similar way as Galactic globular clusters. We also identified 3 out of 11 Si-rich stars with orbital properties completely different compared with the Si-rich component, which have prograde-retrograde orbits at the same time with respect to the direction of the Galactic rotation, more specifically, due to the gravitational effect produced by the bar, further indicating a chaotic behavior (Pérez-Villegas et al. 2018). The remaining stars show orbits expected from an inner-halo population, characterised by high eccentricities ($e > 0.65$) in a prograde sense with respect to the rotation of the bar.

Figure A5 shows a Toomre diagram (the velocities in this dia-

⁴ <https://gravpot.utinam.cnrs.fr>

Table A1. Adopted atmospheric parameters of our target stars, frequency of observation per object (N_{visits}), signal-to-noise (S/N), radial velocity (RV) and radial velocity scatter information (RV_{SCATTER}). \dagger Uncalibrated ASPCAP parameters are listed in columns 7 and 8.

APOGEE ID	[M/H] dex	$J_{2MASS} - K_{s,2MASS}$ mag	E(B-V)	T_{eff}^{pho} K	\log_{10}^{iso} dex	$\text{Teff}^{\dagger}_{\text{ASPCAP}}$ K	$\log_{10}^{\dagger}_{\text{ASPCAP}}$ dex	N_{visits}	S/N pixel $^{-1}$	RV km s $^{-1}$	RV_{SCATTER} km s $^{-1}$
2M13314691+2804210	-1.08	0.907	0.009	4048.1	0.646	4114.6	1.381	4	248	-1.72	0.12
2M15153684+3501283	-0.99	0.77	0.017	4401.3	1.341	4379.2	1.808	3	115	-308.45	0.12
2M16092248+2449223	-1.14	0.971	0.070	3990.5	0.539	4095.6	1.237	5	364	-92.30	0.22
2M16300791+2537503	-1.09	0.67	0.035	4717.5	1.851	4785.8	2.169	2	143	-255.29	0.02
2M16482145-1930487	-0.96	1.013	0.520	4638.1	1.767	4377.4	1.741	3	97	65.98	0.01
2M17155274+2907368	-1.07	0.839	0.058	4287.6	1.076	4313.9	1.601	2	94	-81.42	0.00
2M17214096+4246147	-1.11	0.777	0.020	4385.1	1.249	4439.0	1.614	5	181	-298.07	0.05
2M17502038-2805411	-1.09	3.492	3775.0	0.487	2	101	-53.06	0.13
2M18070782-1517393	-1.07	1.66	3924.7	1.126	3	151	-370.42	0.02
2M19281906+4915086	-1.22	0.79	0.086	4460.6	1.303	4309.0	1.715	3	422	-302.89	0.18
2M23341347+4836321	-1.17	1.027	0.196	4048.9	0.566	4073.1	1.227	3	205	-168.33	0.15

Table A2. Mean elemental abundances derived of our target stars using the "abund" module in `BACCHUS` code, adopting the atmospheric parameters from Payne-APOGEE (abundances labeled as [Fe/H]sp and [X/Fe]sp) and atmospheric parameters from photometry and isochrones (abundances labeled as [Fe/H]pho and [X/Fe]pho). The Solar reference abundances are from (Asplund2005). The `BACCHUS` pipeline was used to derive the broadening parameters, metallicity, and chemical abundances.

APOGEE-ID	[Fe/H]sp	[C/Fe]sp	[N/Fe]sp	[O/Fe]sp	[Mg/Fe]sp	[Al/Fe]sp	[Si/Fe]sp	[Ce/Fe]sp	[Nd/Fe]sp
2M13314691+2804210	-1.07	0.02	0.26	0.43	0.38	0.88	0.85	0.73	...
2M15153684+3501283	-0.99	0.12	0.25	0.43	0.29	0.78	0.81	0.65	...
2M16092248+2449223	-1.11	-0.17	0.38	0.43	0.40	0.86	0.99	0.72	0.77
2M16300791+2537503	-1.04	0.01	0.41	0.50	0.34	0.94	0.78	0.33	...
2M16482145-1930487	-0.99	0.12	0.39	0.50	0.32	0.81	0.81	...	0.89
2M17155274+2907368	-1.07	0.01	0.20	0.41	0.43	...	0.73	0.30	...
2M17214096+4246147	-1.08	-0.16	0.40	0.44	0.46	0.97	1.06	0.76	...
2M17502038-2805411	-1.09	-0.14	0.35	0.42	0.42	...	0.80	0.45	...
2M18070782-1517393	-0.98	0.10	0.15	0.33	0.39	0.70	0.67	0.70	...
2M19281906+4915086	-1.20	-0.21	0.41	0.36	0.20	0.74	0.76
2M23341347+4836321	-1.14	-0.04	0.30	0.40	0.39	0.85	0.80	0.70	...
	[Fe/H]pho	[C/Fe]pho	[N/Fe]pho	[O/Fe]pho	[Mg/Fe]pho	[Al/Fe]pho	[Si/Fe]pho	[Ce/Fe]pho	[Nd/Fe]pho
2M13314691+2804210	-1.23	-0.09	0.44	0.44	0.37	0.77	0.79	0.41	...
2M15153684+3501283	-1.00	-0.01	0.36	0.50	0.51	0.88	0.78	0.38	...
2M16092248+2449223	-1.26	-0.26	0.52	0.35	0.29	0.62	0.81	0.41	0.41
2M16300791+2537503	-1.09	-0.04	0.48	0.48	0.38	0.93	0.83	0.39	...
2M16482145-1930487	-0.89	0.06	0.59	0.81	0.44	0.94	0.69	...	0.81
2M17155274+2907368	-1.14	-0.08	0.33	0.44	0.58	...	0.69	0.32	...
2M17214096+4246147	-1.13	-0.24	0.48	0.42	0.53	0.99	1.05	0.52	...
2M17502038-2805411
2M18070782-1517393
2M19281906+4915086	-1.16	-0.28	0.51	0.63	0.38	0.90	0.67
2M23341347+4836321	-1.22	-0.17	0.47	0.44	0.53	0.92	0.78	0.36	...

gram are relative to the LSR) for Si-rich stars. From inspection, most of Si-rich giant exist in the halo-region of the Toomre diagram, which is dynamically consistent with highly elliptical orbits with eccentricities ($e \gtrsim 0.65$). There are also two Si-rich giants that have disk-like kinematics and are likely with the high-velocity tail of the thick disk (disk-like contaminants).

Figures A7 and A8 shows the orbits for each Si-rich star, using as initial conditions the central values listed in Table A5. For each star, we plotted the projection of the orbit on the Galactic plane (X-Y) and on the meridional plane (R-Z) in the non-inertial reference

frame (columns 2, 3, 4 and 5), where the bar is at rest, and assuming four different patterns speed for the bar, while in the axisymmetric (without bar model) configuration, the orbits are shown in the inertial Galactic frame of reference (column 1).

It is important to mention that one major limitation of our model is that it ignores secular changes in the Milky Way potential over time, which might be important in understanding of the evolution for stars crossing the inner Milky Way. An in-depth analysis of such dynamical behaviour is beyond the scope of this paper.

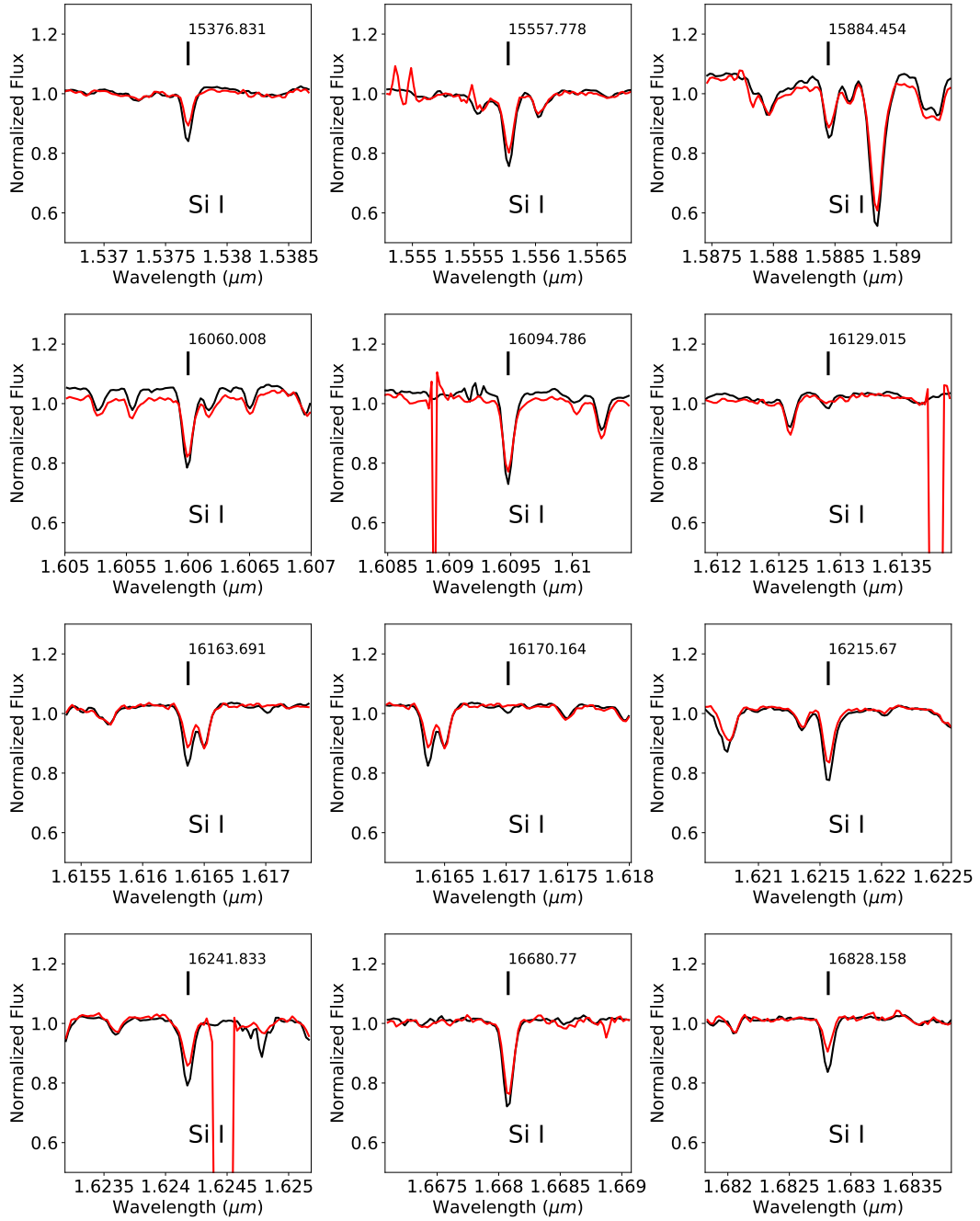


Figure A1. Comparison between the APOGEE spectrum of a normal (red line, star: 2M14424814+4653219, $T_{\text{eff}} = 4346$ K, $\log g = 1.66$, $[\text{Fe}/\text{H}] = -1.19$, $[\text{Si}/\text{Fe}] = +0.25$) and a Si-rich giant star (black line, star: 2M19281906+4915086, $T_{\text{eff}} = 4309$ K, $\log g = 1.71$, $[\text{Fe}/\text{H}] = -1.20$, $[\text{Si}/\text{Fe}] = +0.65$) around the Si I lines, with similar stellar parameters.

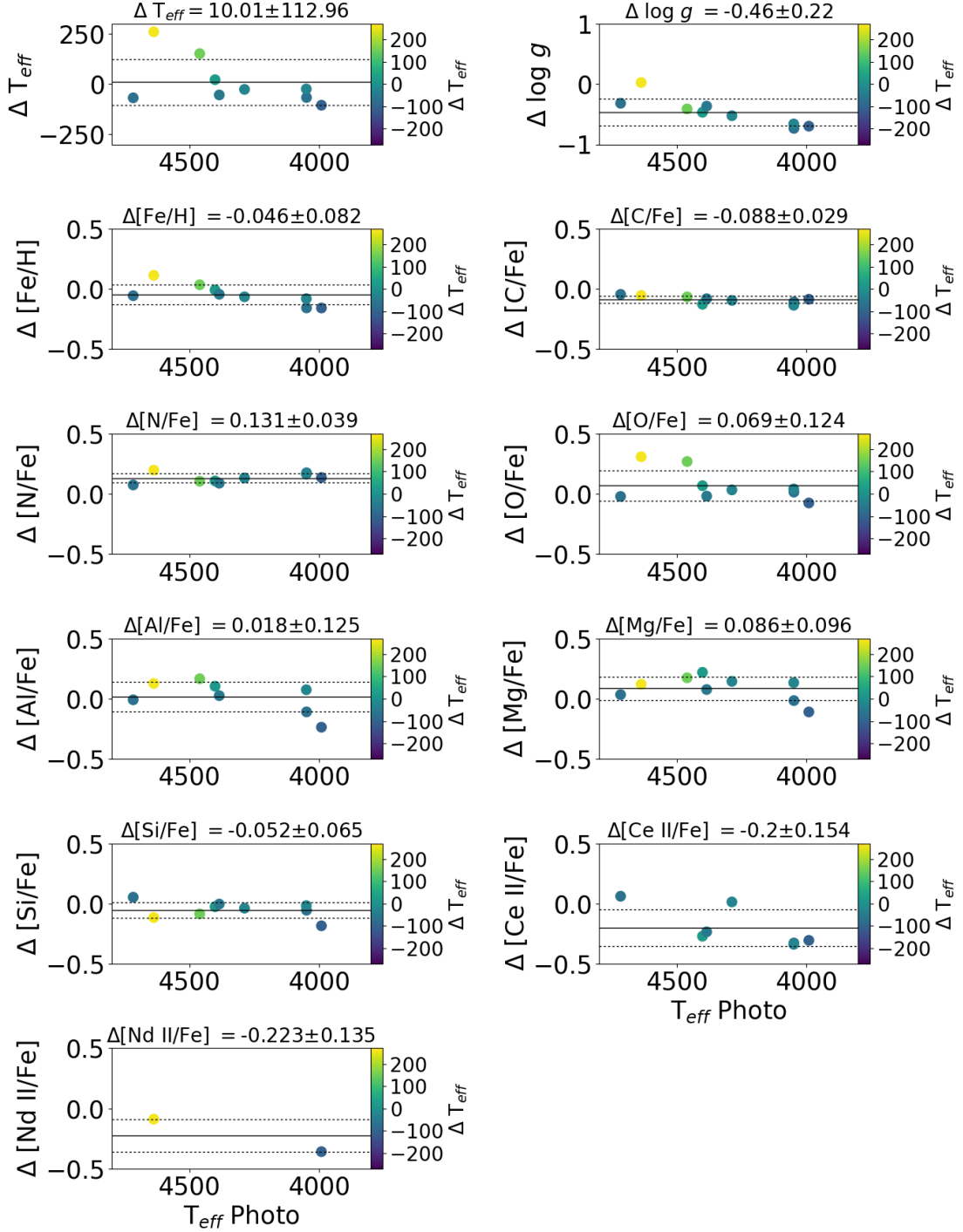


Figure A2. Differences in abundances produced by two runs adopting different temperatures: photometric versus spectroscopic temperatures; otherwise the same calculation method was employed. The symbols are color-coded by the differences between the photometric and spectroscopic temperatures. The average and \pm errors give the standard deviation around the mean of the differences and are listed in the title of each panel.

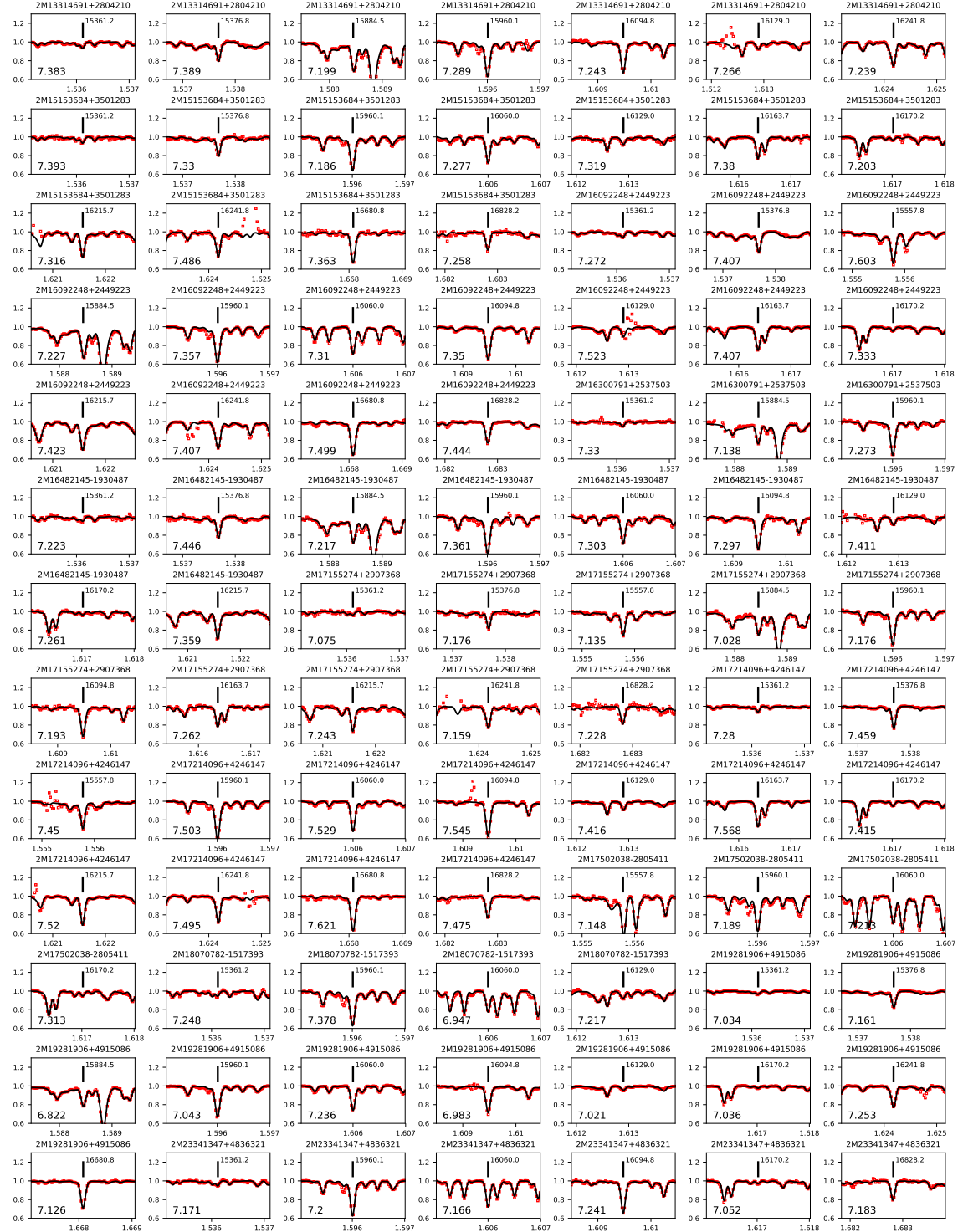


Figure A3. A portion of the APOGEE spectrum (red unfilled squares) and best-fitting LTE model (black line) for the eleven Si-rich giant stars. We mark the positions of the Si I lines and the best-fit abundance values (on the bottom-left corner) per line. Note that the listed best-fit $A(\text{Si I})$ might not be the same as in Table A2, because the table contains averaged values, not individual fits.

Table A3. Abundance determination sensitivity to the stellar parameters for each chemical specie.

APOGEE-ID	X	$\sigma_{[X/H], T_{\text{eff}}}$	$\sigma_{[X/H], \log g}$	$\sigma_{[X/H], \xi_t}$	σ_{mean}	σ_{total}
2M13314691+2804210	Fe	0.049	0.038	0.031	0.067	0.096
2M13314691+2804210	C	0.042	0.098	0.006	0.057	0.121
2M13314691+2804210	N	0.196	0.055	0.021	0.096	0.226
2M13314691+2804210	O	0.160	0.004	0.009	0.041	0.165
2M13314691+2804210	Mg	0.098	0.047	0.042	0.072	0.136
2M13314691+2804210	Al	0.101	0.026	0.017	0.084	0.134
2M13314691+2804210	Si	0.028	0.022	0.035	0.067	0.083
2M13314691+2804210	Ce	0.209	0.157	0.014	0.076	0.272
2M13314691+2804210	Nd
2M15153684+3501283	Fe	0.027	0.012	0.031	0.080	0.090
2M15153684+3501283	C	0.013	0.089	0.006	0.056	0.106
2M15153684+3501283	N	0.112	0.054	0.062	0.110	0.177
2M15153684+3501283	O	0.120	0.006	0.026	0.104	0.161
2M15153684+3501283	Mg	0.062	0.095	0.026	0.104	0.156
2M15153684+3501283	Al	0.085	0.041	0.046	0.005	0.105
2M15153684+3501283	Si	0.006	0.017	0.001	0.083	0.084
2M15153684+3501283	Ce	0.087	0.145	0.004	0.063	0.180
2M15153684+3501283	Nd
2M16092248+2449223	Fe	0.023	0.027	0.091	0.065	0.117
2M16092248+2449223	C	0.016	0.076	0.021	0.109	0.135
2M16092248+2449223	N	0.094	0.036	0.069	0.101	0.158
2M16092248+2449223	O	0.173	0.010	0.034	0.053	0.184
2M16092248+2449223	Mg	0.081	0.044	0.048	0.038	0.110
2M16092248+2449223	Al	0.114	0.027	0.097	0.035	0.156
2M16092248+2449223	Si	0.003	0.107	0.159	0.097	0.214
2M16092248+2449223	Ce	0.059	0.070	0.093	0.046	0.138
2M16092248+2449223	Nd	0.093	0.261	0.108	0.003	0.297
2M16300791+2537503	Fe	0.036	0.007	0.005	0.056	0.067
2M16300791+2537503	C	0.014	0.068	0.003	0.092	0.115
2M16300791+2537503	N	0.112	0.078	0.021	0.085	0.162
2M16300791+2537503	O	0.124	0.023	0.017	0.190	0.228
2M16300791+2537503	Mg	0.088	0.109	0.012	0.067	0.155
2M16300791+2537503	Al	0.085	0.073	0.029	0.061	0.130
2M16300791+2537503	Si	0.068	0.016	0.020	0.080	0.108
2M16300791+2537503	Ce	0.169	0.218	0.004	...	0.275
2M16300791+2537503	Nd
2M16482145-1930487	Fe	0.021	0.009	0.007	0.117	0.119
2M16482145-1930487	C	0.026	0.080	0.009	0.134	0.158
2M16482145-1930487	N	0.087	0.039	0.018	0.094	0.135
2M16482145-1930487	O	0.131	0.004	0.005	0.078	0.152
2M16482145-1930487	Mg	0.052	0.112	0.013	0.069	0.142
2M16482145-1930487	Al	0.062	0.072	0.014	0.069	0.118
2M16482145-1930487	Si	0.009	0.011	0.007	0.075	0.076
2M16482145-1930487	Ce
2M16482145-1930487	Nd	0.036	0.007	0.022	0.062	0.075
2M17155274+2907368	Fe	0.026	0.022	0.017	0.097	0.104
2M17155274+2907368	C	0.025	0.076	0.036	0.182	0.202
2M17155274+2907368	N	0.097	0.050	0.054	0.146	0.190
2M17155274+2907368	O	0.137	0.007	0.014	0.094	0.166
2M17155274+2907368	Mg	0.083	0.073	0.027	0.095	0.148
2M17155274+2907368	Al
2M17155274+2907368	Si	0.003	0.041	0.035	0.069	0.087
2M17155274+2907368	Ce	0.148	0.200	0.169	...	0.300
2M17155274+2907368	Nd
2M17214096+4246147	Fe	0.037	0.013	0.029	0.059	0.076
2M17214096+4246147	C	0.016	0.077	0.010	0.136	0.157
2M17214096+4246147	N	0.086	0.033	0.038	0.078	0.126
2M17214096+4246147	O	0.140	0.017	0.023	0.079	0.163
2M17214096+4246147	Mg	0.079	0.065	0.033	0.066	0.126
2M17214096+4246147	Al	0.087	0.033	0.037	0.034	0.105
2M17214096+4246147	Si	0.017	0.025	0.057	0.081	0.103
2M17214096+4246147	Ce	0.049	0.112	0.030	0.093	0.156
2M17214096+4246147	Nd
2M17502038-2805411	Fe	0.068	0.093	0.031	0.128	0.174
2M17502038-2805411	C	0.008	0.070	0.006	0.049	0.086
2M17502038-2805411	N	0.137	0.023	0.033	0.197	0.243
2M17502038-2805411	O	0.241	0.069	0.038	0.074	0.264
2M17502038-2805411	Mg	0.198	0.168	0.043	0.063	0.270
2M17502038-2805411	Al
2M17502038-2805411	Si	0.063	0.122	0.025	0.060	0.151
2M17502038-2805411	Ce	0.177	0.223	0.011	0.060	0.291
2M17502038-2805411	Nd

Table A4. (Continued.)

APOGEE-ID	X	$\sigma_{[X/H], T_{\text{eff}}}$	$\sigma_{[X/H], \log g}$	$\sigma_{[X/H], \xi_t}$	σ_{mean}	σ_{total}
2M18070782-1517393	Fe	0.016	0.016	0.090	0.094	0.132
2M18070782-1517393	C	0.004	0.113	0.011	0.088	0.143
2M18070782-1517393	N	0.132	0.068	0.138	0.119	0.235
2M18070782-1517393	O	0.140	0.005	0.057	0.064	0.164
2M18070782-1517393	Mg	0.053	0.082	0.093	0.175	0.220
2M18070782-1517393	Al	0.063	0.044	0.095	0.031	0.126
2M18070782-1517393	Si	0.012	0.016	0.049	0.156	0.164
2M18070782-1517393	Ce	0.072	0.195	0.036	0.11	0.237
2M18070782-1517393	Nd
2M19281906+4915086	Fe	0.025	0.023	0.018	0.061	0.072
2M19281906+4915086	C	0.017	0.080	0.035	0.201	0.219
2M19281906+4915086	N	0.092	0.030	0.025	0.077	0.126
2M19281906+4915086	O	0.146	0.010	0.017	0.074	0.164
2M19281906+4915086	Mg	0.073	0.050	0.029	0.153	0.179
2M19281906+4915086	Al	0.050	0.026	0.026	0.073	0.095
2M19281906+4915086	Si	0.014	0.013	0.008	0.121	0.122
2M19281906+4915086	Ce
2M19281906+4915086	Nd
2M23341347+4836321	Fe	0.014	0.019	0.006	0.067	0.071
2M23341347+4836321	C	0.009	0.086	0.076	0.108	0.157
2M23341347+4836321	N	0.122	0.045	0.003	0.111	0.170
2M23341347+4836321	O	0.153	0.009	0.003	0.055	0.162
2M23341347+4836321	Mg	0.075	0.072	0.014	0.041	0.112
2M23341347+4836321	Al	0.095	0.041	0.051	0.034	0.120
2M23341347+4836321	Si	0.003	0.006	0.017	0.057	0.059
2M23341347+4836321	Ce	0.029	0.164	0.037	0.106	0.200
2M23341347+4836321	Nd

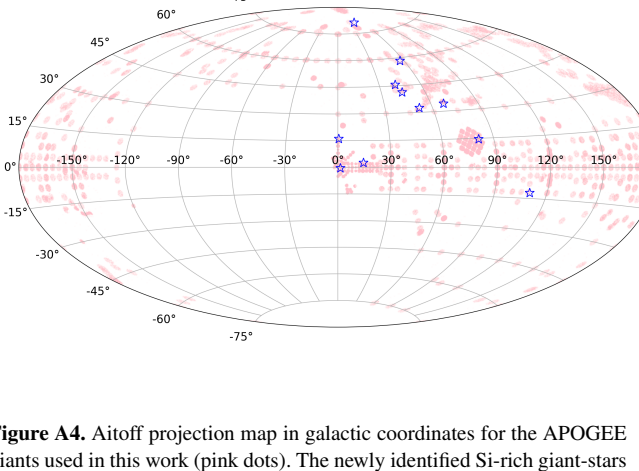


Figure A4. Aitoff projection map in galactic coordinates for the APOGEE giants used in this work (pink dots). The newly identified Si-rich giant-stars are highlighted with blue 'star' symbols.

Table A5. Monte Carlo orbital elements of eleven Si-Al-rich stars. The average value of the orbital elements (pericentric and apocentric radii, the eccentricity, the maximum distance the orbit reaches above/below the Galactic plane and the minimum/maximum value of the z-component of the angular momentum in the inertial frame) was found for the one million realizations, with uncertainty ranges given by the 16th (subscript) and 84th (superscript) percentile values.

Ω_{bar} km s ⁻¹ kpc ⁻¹	APOGEE-ID	α [$^{\circ}$]	δ [$^{\circ}$]	RV $\pm\Delta$ km s ⁻¹	$\mu_{\alpha}\pm\Delta$ mas yr ⁻¹	$\mu_{\delta}\pm\Delta$ mas yr ⁻¹	d $\pm\Delta$ kpc	$\langle r_{peri} \rangle$ kpc	$\langle r_{apo} \rangle$ kpc	$\langle e \rangle$	$\langle Z_{max} \rangle$ kpc	$\langle L_{z,min} \rangle$ $\times 10 \text{ km s}^{-1} \text{ kpc}^{-1}$	$\langle L_{z,max} \rangle$ $\times 10 \text{ km s}^{-1} \text{ kpc}^{-1}$
35	2M13314691+2804210	202.945464	28.07251	-1.70 ± 0.13	-7.32 ± 0.07	-6.54 ± 0.03	5.78 ± 0.56	$0.11^{+0.68}_{-0.03}$	$9.91^{+10.61}_{-9.63}$	$0.97^{+0.99}_{-0.87}$	$6.75^{+7.73}_{-5.45}$	$2.02^{+3.0}_{-15.0}$	$22.0^{+46.2}_{-14.0}$
40	$0.24^{+0.73}_{-0.02}$	$9.93^{+10.49}_{-9.73}$	$0.95^{+0.99}_{-0.87}$	$6.33^{+6.89}_{-5.60}$	$4.02^{+5.0}_{-10.0}$	$21.0^{+40.0}_{-10.0}$
45	$0.31^{+0.59}_{-0.04}$	$10.04^{+10.61}_{-9.64}$	$0.94^{+0.99}_{-0.89}$	$6.40^{+5.71}_{-5.57}$	$6.0^{+19.0}_{-26.0}$	$19.0^{+37.0}_{-3.0}$
50	$0.08^{+0.58}_{-0.02}$	$10.13^{+11.56}_{-9.38}$	$0.98^{+0.99}_{-0.89}$	$7.28^{+8.21}_{-6.14}$	$-1.0^{+19.2}_{-14.0}$	$15.0^{+38.0}_{-3.0}$
35	2M15153684+3501283	228.903514	35.024532	-308.86 ± 0.05	-4.14 ± 0.02	-7.74 ± 0.03	9.65 ± 1.97	$1.74^{+1.85}_{-1.83}$	$22.11^{+35.32}_{-31.89}$	$0.84^{+0.90}_{-0.80}$	$18.28^{+36.38}_{-36.89}$	$74.0^{+78.0}_{-62.0}$	$80.0^{+84.0}_{-88.0}$
40	$1.74^{+1.88}_{-1.88}$	$23.05^{+32.88}_{-31.86}$	$0.85^{+0.90}_{-0.80}$	$19.0^{+66.0}_{-51.0}$	$74.0^{+66.0}_{-66.0}$	$79.0^{+88.0}_{-88.0}$
45	$1.73^{+1.89}_{-1.89}$	$22.67^{+35.18}_{-35.18}$	$0.88^{+0.90}_{-0.90}$	$19.18^{+35.57}_{-35.57}$	$73.0^{+76.0}_{-76.0}$	$79.0^{+82.0}_{-82.0}$
50	$1.72^{+1.80}_{-1.88}$	$23.03^{+35.68}_{-35.68}$	$0.87^{+0.91}_{-0.80}$	$19.85^{+35.96}_{-35.96}$	$73.0^{+64.0}_{-64.0}$	$79.0^{+82.0}_{-82.0}$
35	2M16092248+2449223	242.34367	24.82286	-92.18 ± 0.44	-9.28 ± 0.03	-1.51 ± 0.04	6.36 ± 0.70	$0.51^{+1.20}_{-1.12}$	$9.32^{+9.71}_{-8.62}$	$0.89^{+0.96}_{-0.97}$	$7.26^{+8.03}_{-8.07}$	$17.0^{+43.0}_{-38.0}$	$36.0^{+59.0}_{-52.0}$
40	$0.70^{+1.11}_{-0.11}$	$9.17^{+9.86}_{-8.86}$	$0.82^{+0.90}_{-0.78}$	$6.60^{+6.11}_{-5.95}$	$25.5^{+40.0}_{-40.0}$	$43.5^{+18.0}_{-18.0}$
45	$0.69^{+1.14}_{-0.14}$	$9.17^{+9.80}_{-8.80}$	$0.86^{+0.92}_{-0.86}$	$7.11^{+5.58}_{-5.58}$	$22.0^{+40.0}_{-40.0}$	$36.0^{+50.0}_{-50.0}$
50	$0.62^{+1.30}_{-0.18}$	$9.18^{+10.02}_{-8.76}$	$0.87^{+0.96}_{-0.75}$	$7.29^{+8.27}_{-5.95}$	$19.0^{+34.0}_{-3.0}$	$34.0^{+54.2}_{-19.0}$
35	2M16300791+2537503	247.532999	25.630659	-255.37 ± 0.05	-3.02 ± 0.02	-9.40 ± 0.02	4.72 ± 0.35	$0.40^{+0.53}_{-0.43}$	$7.97^{+8.32}_{-8.32}$	$0.89^{+0.89}_{-0.87}$	$7.84^{+7.93}_{-7.93}$	$14.0^{+15.0}_{-13.0}$	$29.0^{+32.0}_{-32.0}$
40	$0.50^{+0.60}_{-0.60}$	$7.53^{+8.00}_{-7.80}$	$0.86^{+0.87}_{-0.85}$	$7.19^{+7.28}_{-7.28}$	$17.0^{+19.0}_{-14.0}$	$36.0^{+39.0}_{-34.0}$
45	$0.50^{+0.34}_{-0.34}$	$7.96^{+8.74}_{-8.74}$	$0.87^{+0.89}_{-0.86}$	$8.09^{+8.33}_{-8.33}$	$11.0^{+6.0}_{-6.0}$	$33.0^{+21.0}_{-21.0}$
50	$0.37^{+0.46}_{-0.19}$	$8.36^{+9.48}_{-8.61}$	$0.90^{+0.98}_{-0.98}$	$8.21^{+10.1}_{-7.99}$	$9.0^{+2.0}_{-1.0}$	$23.0^{+24.0}_{-22.0}$
35	2M16482145-1930487	252.089408	-19.513531	66.38 ± 0.76	-0.11 ± 0.06	-10.05 ± 0.03	5.49 ± 0.38	$0.08^{+0.14}_{-0.01}$	$4.85^{+5.21}_{-4.60}$	$0.98^{+0.99}_{-0.94}$	$3.10^{+3.36}_{-2.16}$	$-27.0^{+24.0}_{-34.0}$	$3.0^{+12.0}_{-3.0}$
40	$0.10^{+0.35}_{-0.03}$	$4.89^{+5.26}_{-4.56}$	$0.94^{+0.98}_{-0.87}$	$2.61^{+3.44}_{-2.22}$	$-27.0^{+21.0}_{-37.0}$	$-3.0^{+6.0}_{-11.0}$
45	$0.10^{+0.33}_{-0.02}$	$4.82^{+5.15}_{-4.53}$	$0.95^{+0.98}_{-0.87}$	$2.47^{+3.25}_{-2.09}$	$-27.0^{+18.0}_{-34.0}$	$0.6^{+7.0}_{-10.0}$
50	$0.30^{+0.39}_{-0.14}$	$4.94^{+5.46}_{-4.71}$	$0.88^{+0.94}_{-0.85}$	$2.68^{+3.07}_{-2.24}$	$-30.0^{+25.0}_{-38.0}$	$-9.0^{+2.0}_{-12.0}$
35	2M17155274+2907368	258.969764	29.126892	-81.52 ± 0.02	-4.11 ± 0.02	-1.87 ± 0.03	7.67 ± 0.61	$0.80^{+0.97}_{-0.78}$	$8.51^{+8.99}_{-8.28}$	$0.81^{+0.83}_{-0.79}$	$5.02^{+5.93}_{-5.58}$	$-46.0^{+41.0}_{-54.0}$	$-31.0^{+28.0}_{-32.0}$
40	$0.80^{+0.94}_{-0.59}$	$8.51^{+8.34}_{-8.34}$	$0.82^{+0.87}_{-0.80}$	$4.81^{+5.58}_{-4.47}$	$-46.0^{+41.0}_{-51.0}$	$-30.0^{+30.0}_{-33.0}$
45	$0.90^{+1.17}_{-0.82}$	$8.73^{+8.96}_{-8.53}$	$0.79^{+0.83}_{-0.75}$	$4.83^{+5.77}_{-4.30}$	$-52.0^{+44.0}_{-59.0}$	$-37.0^{+43.0}_{-43.0}$
50	$1.03^{+1.22}_{-0.82}$	$9.97^{+10.15}_{-9.37}$	$0.81^{+0.84}_{-0.77}$	$5.82^{+6.20}_{-4.28}$	$-60.0^{+53.0}_{-66.0}$	$-37.0^{+30.0}_{-43.0}$
35	2M17214096+4246147	260.420668	42.770763	-298.07 ± 0.03	-5.60 ± 0.04	-3.97 ± 0.05	6.43 ± 1.13	$1.36^{+1.46}_{-1.40}$	$9.54^{+10.89}_{-9.73}$	$0.74^{+0.79}_{-0.74}$	$5.04^{+7.11}_{-5.93}$	$50.0^{+53.0}_{-44.0}$	$63.0^{+66.0}_{-88.0}$
40	$1.31^{+1.11}_{-1.11}$	$9.91^{+9.28}_{-8.28}$	$0.76^{+0.75}_{-0.75}$	$5.32^{+5.93}_{-4.79}$	$49.0^{+41.0}_{-41.0}$	$63.0^{+58.0}_{-58.0}$
45	$1.41^{+1.48}_{-1.41}$	$9.84^{+11.94}_{-8.86}$	$0.74^{+0.83}_{-0.83}$	$4.16^{+5.25}_{-4.25}$	$52.0^{+54.0}_{-54.0}$	$64.0^{+68.0}_{-68.0}$
50	$1.30^{+1.09}_{-0.98}$	$10.10^{+9.21}_{-9.00}$	$0.75^{+0.77}_{-0.72}$	$4.25^{+3.77}_{-3.77}$	$50.0^{+40.0}_{-40.0}$	$66.0^{+63.0}_{-63.0}$
35	2M17502038-2805411	267.58493	-28.094751	-53.01 ± 0.25	1.49 ± 3.30	-7.81 ± 2.56	4.77 ± 0.79	$0.83^{+1.96}_{-0.11}$	$3.97^{+5.02}_{-3.09}$	$0.68^{+0.93}_{-0.38}$	$1.68^{+2.75}_{-0.43}$	$-54.0^{+33.0}_{-78.0}$	$-22.0^{+2.0}_{-50.0}$
40	$0.74^{+1.00}_{-0.99}$	$4.08^{+5.07}_{-4.07}$	$0.68^{+0.94}_{-0.92}$	$1.66^{+2.18}_{-1.18}$	$-57.0^{+37.0}_{-84.0}$	$-19.5^{+46.0}_{-46.0}$
45	$0.66^{+1.98}_{-0.10}$	$4.13^{+5.09}_{-4.13}$	$0.69^{+0.94}_{-0.43}$	$1.65^{+2.46}_{-1.46}$	$-59.0^{+31.0}_{-42.0}$	$-18.0^{+48.2}_{-48.2}$
50	$0.73^{+1.92}_{-0.14}$	$4.01^{+5.36}_{-3.19}$	$0.68^{+0.92}_{-0.45}$	$1.59^{+2.73}_{-0.49}$	$-60.0^{+33.0}_{-88.0}$	$-18.0^{+47.0}_{-47.0}$
35	2M18070782-1517393	271.782601	-15.294253	-369.91 ± 0.01	-2.86 ± 0.18	-1.48 ± 0.15	4.54 ± 1.34	$0.07^{+0.53}_{-0.02}$	$12.20^{+15.84}_{-10.09}$	$0.98^{+0.99}_{-0.93}$	$0.47^{+0.79}_{-0.35}$	$-20.0^{+13.0}_{-39.0}$	$1.0^{+32.2}_{-27.0}$
40	$0.10^{+0.58}_{-0.64}$	$12.66^{+15.79}_{-16.28}$	$0.97^{+0.99}_{-0.99}$	$0.47^{+0.77}_{-0.77}$	$-19.5^{+37.0}_{-11.0}$	$8.0^{+29.0}_{-29.0}$
45	$0.10^{+0.02}_{-0.02}$	$12.26^{+12.68}_{-8.86}$	$0.98^{+0.99}_{-0.99}$	$0.46^{+0.68}_{-0.68}$	$-13.0^{+44.2}_{-44.2}$	$1.0^{+25.0}_{-25.0}$
50	$0.29^{+0.69}_{-0.03}$	$14.14^{+16.12}_{-9.11}$	$0.95^{+0.99}_{-0.91}$	$0.46^{+1.07}_{-0.35}$	$-29.0^{+9.0}_{-43.0}$	$10.0^{+34.0}_{-21.0}$
35	2M19281906+4915086	292.079441	49.252403	-302.26 ± 0.09	-11.38 ± 0.05	-0.92 ± 0.05	3.78 ± 0.33	$1.35^{+1.43}_{-1.44}$	$9.47^{+10.08}_{-9.13}$	$0.78^{+0.78}_{-0.73}$	$7.15^{+8.30}_{-8.30}$	$46.0^{+50.0}_{-40.0}$	$61.0^{+68.0}_{-64.0}$
40	$1.41^{+1.36}_{-1.36}$	$9.41^{+9.26}_{-9.26}$	$0.73^{+0.72}_{-0.72}$	$6.71^{+8.57}_{-8.57}$	$48.5^{+44.0}_{-44.0}$	$61.0^{+57.0}_{-57.0}$
45	$1.37^{+1.36}_{-1.36}$	$9.55^{+9.29}_{-9.29}$	$0.74^{+0.74}_{-0.74}$	$7.15^{+8.34}_{-8.34}$	$47.0^{+44.0}_{-44.0}$	$58.0^{+63.0}_{-63.0}$
50	$1.38^{+1.06}_{-1.06}$	$9.76^{+9.29}_{-9.29}$	$0.73^{+0.72}_{-0.72}$	$7.36^{+6.29}_{-6.29}$	$47.0^{+40.0}_{-40.0}$	$60.0^{+54.0}_{-54.0}$
35	2M23341347+4836321	353.556144	48.60894	-168.24 ± 0.12	2.28 ± 0.03	-0.43 ± 0.03	11.31 ± 1.32	$0.28^{+0.69}_{-0.04}$	$16.79^{+19.53}_{-15.45}$	$0.96^{+0.99}_{-0.91}$	$2.99^{+4.42}_{-2.41}$	$-31.0^{+16.0}_{-49.0}$	$-8.0^{+15.2}_{-33.0}$
40	$0.29^{+0.70}_{-0.08}$	$17.62^{+16.22}_{-16.22}$	$0.96^{+0.99}_{-0.91}$	$3.34^{+4.54}_{-4.54}$	$-36.0^{+4.0}_{-54.0}$	$-12.0^{+4.0}_{-34.0}$
45	$0.37^{+0.15}_{-0.15}$	$17.33^{+20.44}_{-15.76}$	$0.95^{+0.98}_{-0.91}$	$3.16^{+4.22}_{-2.43}$	$-34.0^{+0.0}_{-53.0}$	$-17.0^{+48.2}_{-34.0}$
50	$0.40^{+0.74}_{-0.10}$	$18.55^{+19.23}_{-15.99}$	$0.94^{+0.98}_{-0.91}$	$2.95^{+4.07}_{-2.42}$	$-38.0^{+8.0}_{-57.0}$	$-21.0^{+11.0}_{-37.0}$

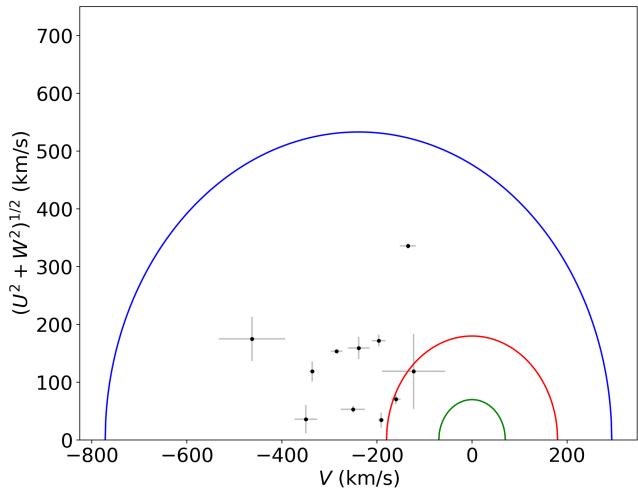


Figure A5. Toomre diagram for Si-rich giants. The green and blue rings show roughly the boundaries of the thin and thick disk at a constant velocity of 70 km s^{-1} and 180 km s^{-1} , respectively. A constant galactic rest frame velocity of 533 km s^{-1} is shown by the blue solid line, and shifted relative to the other velocities. We can see that most of our Si-rich stars belong to the halo kinematically.

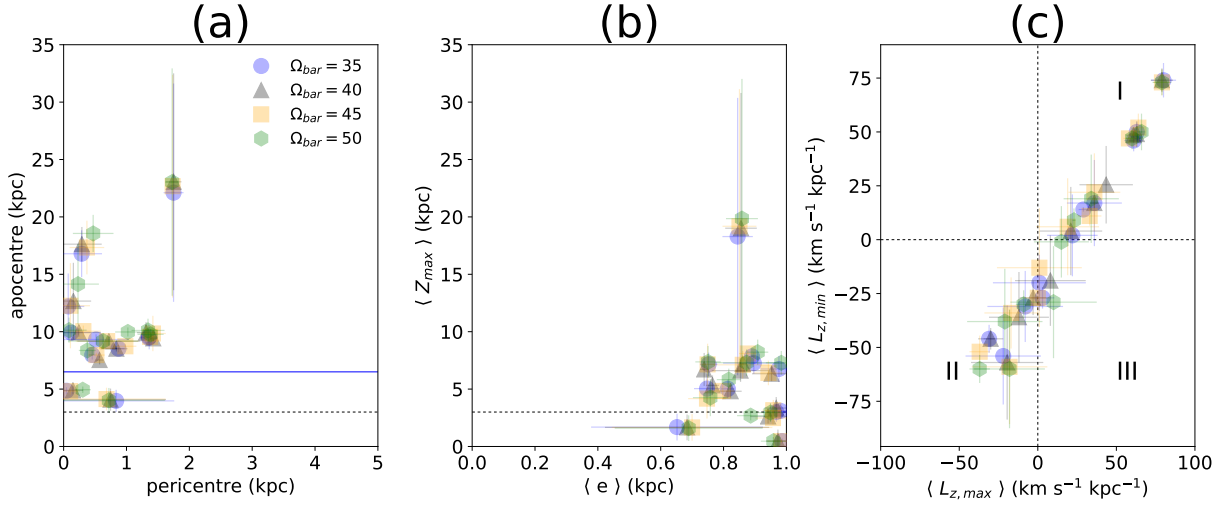


Figure A6. Orbital parameters calculated with different assumed patterns speed for the bar, 35 (blue circles), 40 (grey triangles), 45 (orange squares), and 50 (green hexagons) $\text{km s}^{-1} \text{kpc}^{-1}$. In panel (a), the shaded region and the black dotted line indicates the radius (3 kpc; Barbuy et al. 2018) of the Milky Way bulge, while the blue line indicates the location of the bar's corotation radius ($\text{CR} \sim 6.5$ kpc). For panel (a), a star below the black dotted line would have a bulge-like orbit. In panel (b), the black dotted line represents the edge Z_{max} of the thick disk (~ 3 kpc, Carollo 2010). In panel (c), the black dotted lines divide the regions with prograde orbits (region *II*) with respect to the direction of the Galactic rotation, retrograde orbits (*region I*), and stars that have prograde-retrograde orbits at the same time (*region III*). The error bars show the uncertainty in the computed orbital parameters.

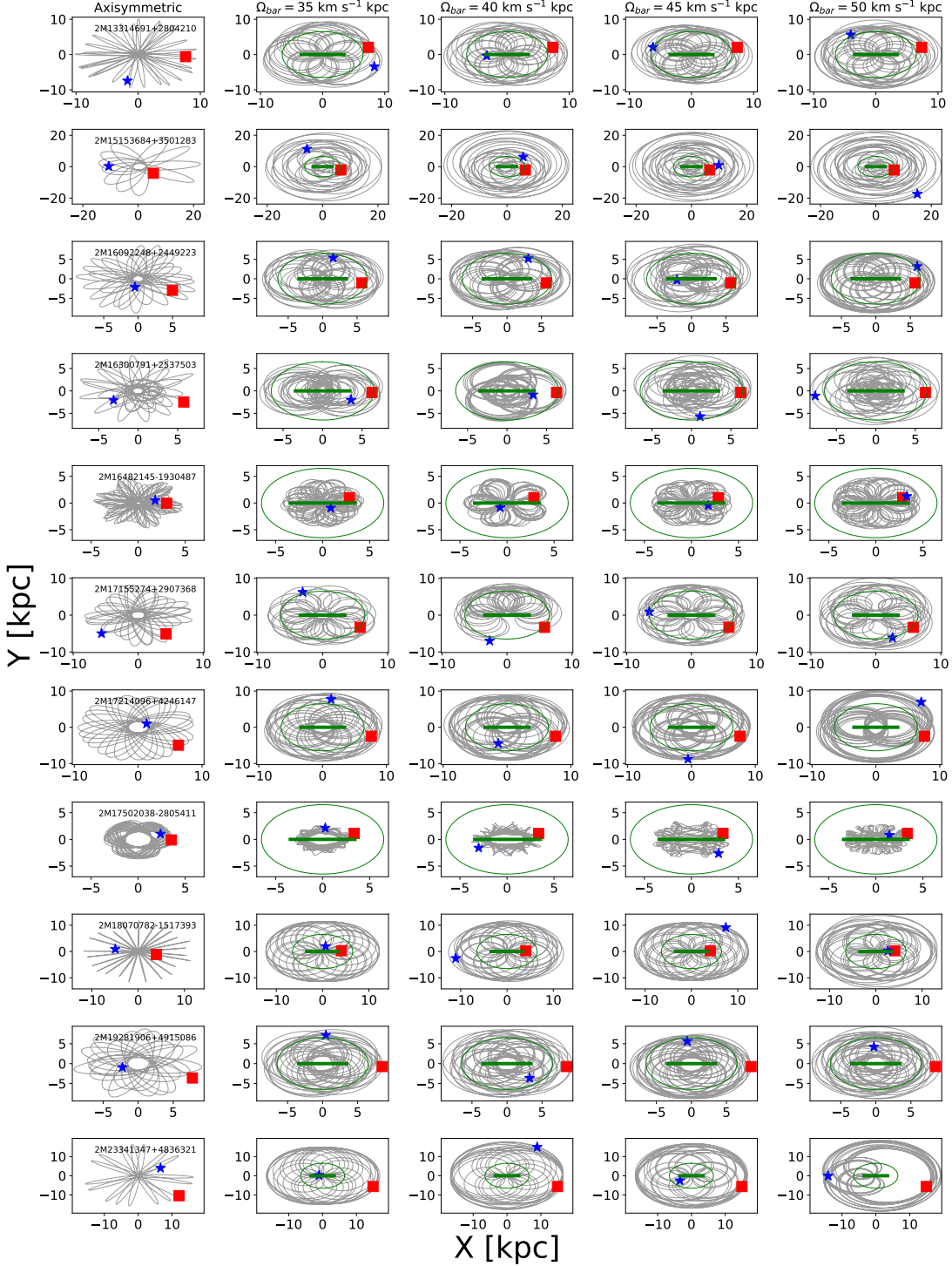


Figure A7. Orbita for the sample of Si-Al-rich stars in an x–y projection, integrated adopting the central values (positions, proper motions, radial velocity, and distance) in both an axisymmetric model (*column 1*), and for models including the Galactic bar potential in the *noninertial* reference frame, where the bar is at rest (*columns 2, 3 and 4*). The green solid line show the size of the Galactic bar, and the large green circle the co-rotation radius, CR ~ 6.5 kpc. The small red square symbols mark the present position of the star, and the blue star symbols mark its final position.

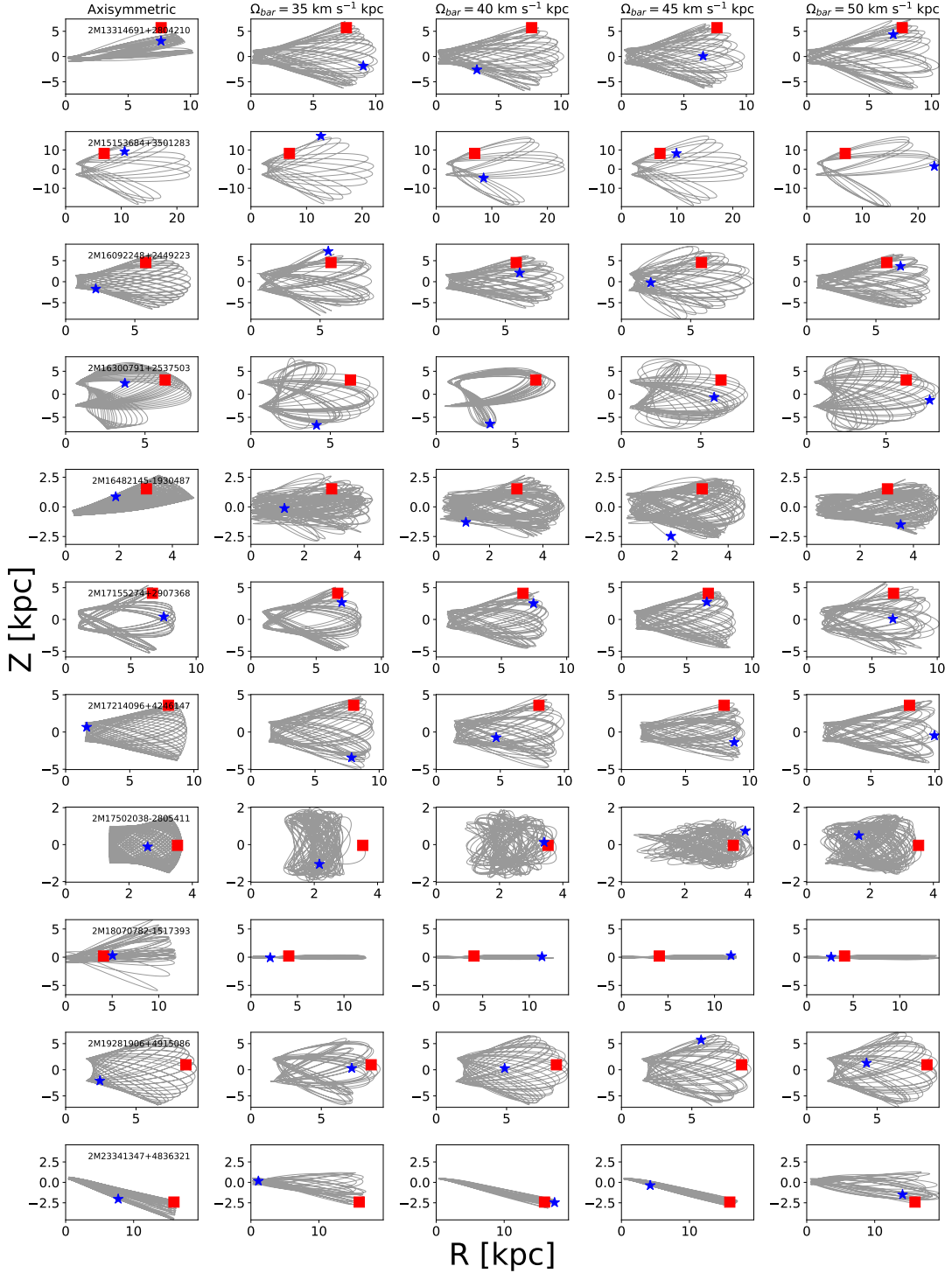


Figure A8. Orbit for the same sample in an R–z projection. The symbols have the same meaning as those in Figure A7.